KØBENHAVNS UNIVERSITET

Master's thesis

Jon Arrizabalaga-Iriarte
Lide Lejonagoitia-Garmendia

Firn densification under arbitrary stresses

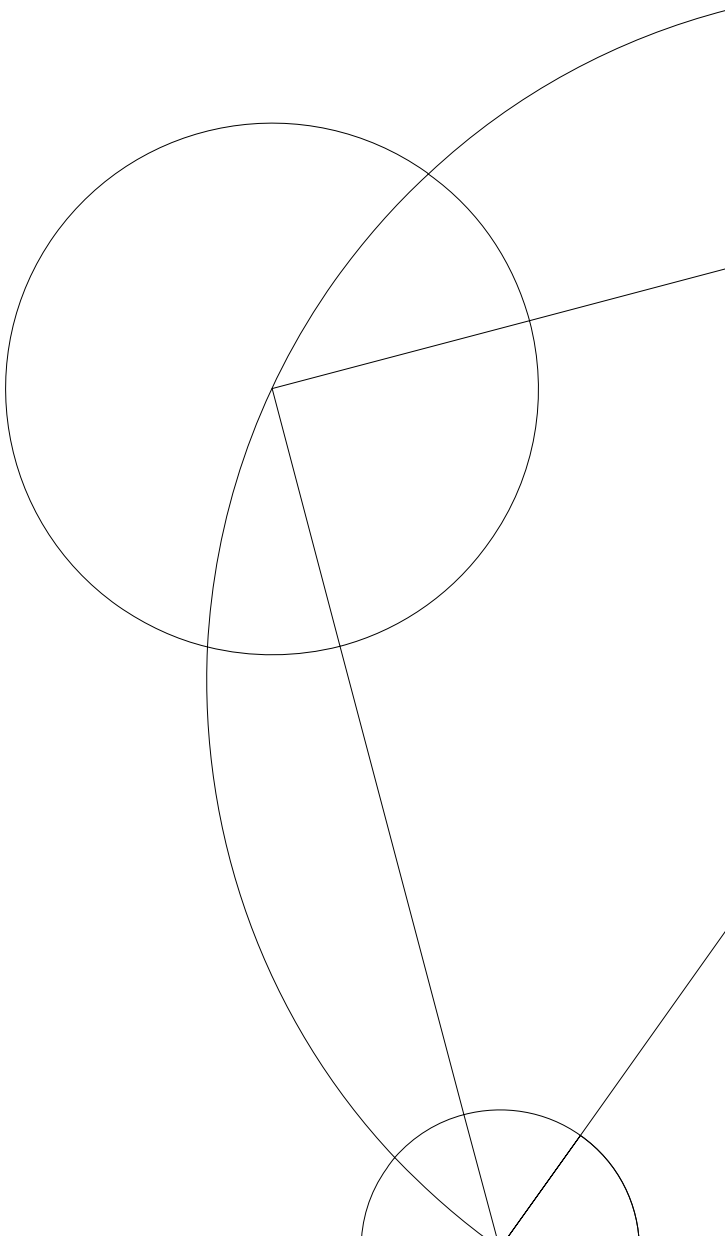

Supervisors

Aslak Grinsted
Christine S. Hvidberg
Nicholas M. Rathmann

External censor

Sebastian B. Simonsen

Copenhagen, 31st October 2022

Abstract

Firn densification refers to the transformation of snow into ice, a process that directly impacts the interpretation of past climatic records from ice cores and mass-loss estimates from altimetry data, among others. This compaction is driven by a complex combination of mechanisms yet to be understood, which compels the use of empirical models that usually assume the absence of horizontal stresses. However, Gagliardini and Meyssonnier (1997) developed a compressible porous law that describes how firn deforms when exposed to arbitrary stress configurations. In this project, we have recalibrated this semi-empirical model by extending the analysis to *in-situ* depth-density measurements from six Greenlandic sites. The results of this calibration process are compatible with a universal set of model parameters but suggest that the widely used original values can be improved by a more extensive study like this. After the calibration, we have found that the densification model can only reproduce the shallower firn columns found around the shear margins of the Northeast Greenland Ice Stream if the horizontal stresses are considered. This result shows that the stress-induced strain softening affects the densification rates and, thus, firn densification models should be forced not only by the accumulation rate and temperature but by the horizontal stresses as well. Finally, we propose a method that can give insights into potential structural improvements that maximize the durability of future firn tunnels. We have found that, consistent with field observations, this optimization scheme favors narrower tunnels with an arch-like ceiling, and supports the idea of filling additional *supporting walls* around.

Contents

List of Figures

Part I

Introduction and Theoretical Background

1. Introduction

Ice sheets and glaciers cover around 10% of Earth's land area (Abram et al., 2019). They only account for the 1.74% of the total amount of water on Earth (Gleick, 1996), but it would be enough to raise the global sea level by more than 60 meters if they completely melted (NASA, 2021). However, glaciers' and ice sheets' interaction with the Earth system goes beyond that of sea-level rise and significantly impacts the climate system. For example, their high albedo affects the global energy budget, and the release of freshwater from ice sheets to the ocean is one of the main drivers of the deep oceanic circulation (Cuffey and Paterson, 2010). It is clear, then, that ice sheets and glaciers are key components of the Earth system.

There may be a tendency to imagine ice sheets and glaciers as huge pure-ice slabs. However, although this representation is adequate for large-scale ice flow modeling (Gerber et al., 2021; Winkelmann et al., 2011), it does not hold for the upper 50-150 meters, where the precipitated snow is still transforming into ice. The matter in this intermediate state is called *firn* and, thus, the aforementioned surface layer is known as *firn zone* or *layer*. Besides, since the main indicator of this transformation process is an increase of density (from that of snow up to that of ice), the whole compaction process is denominated *firn densification*. As we shall see, some firn densification properties are interesting in both ice core dating and altimetry studies.

Ice cores drilled in glaciers and ice sheets are one of the most detailed records of past climatic conditions, containing information about atmospheric composition, dust transport, or volcanic activity, among many others. Although most of the data is retrieved from deep in the ice sheets, understanding the surface layer's processes is crucial for interpreting some of the magnitudes. The most evident example is the gas-related measurements since the air only becomes isolated from the atmosphere deep in the firn column, at the so-called bubble close-off depth. This creates an age difference of 100-1000 years between the trapped gases and the surrounding ice (Δage), which must be considered to synchronize the data properly (Schwander et al., 1997).

Another case where understanding firn densification becomes critical is when estimating the mass of the ice sheet from its height. This is especially important for studies that try to monitor the mass balance from altimetry data. Since the aim is to translate changes in altitude into mass changes, any effect that impacts the height without a corresponding mass loss must be considered first. One such process is, indeed, the compression of firn under its own weight, and it has been estimated that neglecting its effect results in around a 10% increase in the mass loss calculation (Sørensen et al., 2011). Consequently, any other magnitude derived from these estimates is also affected by this bias, e.g. sea-level rise estimates (Lipovsky, 2022).

This way, the importance of firn models becomes evident since they are the most straightforward tool to estimate both the bubble close-off (BC0) depth and the densification rate, relevant for the interpretation of climatic records from ice cores and mass-loss estimates. However, firn densification is a complex process in which the crystals rearrange and change their shape and size. The relative importance of the mechanisms behind these modifications varies with density, so the densification process is divided into different stages depending on the prevailing one (Cuffey and Paterson, 2010). Unfortunately, a theory linking snow to pure ice is still missing because the process is so complex. Moreover, until now, none of the proposed phenomenological models have succeeded in reproducing the data observed at sites with diverse conditions (temperature, accumulation, or mechanical stresses, e.g.). On top of that, different models often give inconsistent predictions for the same physical system (Lundin et al., 2017).

Until now, most of the proposed firn densification models have been empirical, and they implicitly assume the absence of horizontal stresses. However, Gagliardini and Meyssonnier (1997) developed a model that simulates the densification and deformation of firn under arbitrary stress configurations. The model is based on a compressible porous law for firn, which was adapted to fit *in-situ* measured density profiles from Site-2, Greenland. The first aim of this Master's Thesis is to try to improve the Gagliardini and Meyssonnier (1997) model by recalibrating it to a wider range of field data. After this, the model has been applied to analyze the deformation of firn tunnels over time and the possible effect of strain softening on surface elevation and the densification rate.

This report has been divided into three main parts: Introduction and Theoretical Background (Chapters 1-4), Methods and Results (Chapters 5-8), and Discussion and Conclusions (Chapters 9-10). Chapter 2 reviews the physics behind firn densification and its modeling. Then, the governing equations and rheology are shown in Chapter 3. As these equations have been solved based on the Finite Element Method (FEM), a brief introduction to it is provided in Chapter 4. After that, the models used during the project are described in Chapter 5, and the results of the validation of the model, the optimization problem, and the analysis of the strain-softening effect are presented in Chapters 6, 7, and 8 respectively. The report will conclude with a discussion about the results, their conclusions, and a final outlook for future work in Chapters 9 and 10.

2. Firn densification

The purpose of this chapter is to review firn densification, that is, the process through which snow precipitated on glaciers and ice sheets becomes glacial ice. First of all, the mechanisms behind this complex process will be discussed. Then, external factors affecting the density profile will be pointed out. Finally, some of the main firn densification models will be presented.

2.1 Firn densification mechanisms

Crystals rearrange and change their shape and size during the transformation of snow into ice. These modifications are driven by several mechanisms whose relative importance varies with density; therefore, the whole densification process is divided into different stages depending on the prevailing one (see Figure 3.1).

The first stage corresponds to the rapid densification of highly porous firn ($\rho < 550\,\mathrm{kg\,m^{-3}}$), characterized by the settling down and rounding of the grains. The grain boundary sliding dominates this initial densification, that is, the rearrangement of grains by sliding against each other due to the overburden pressure (Alley, 1987). When snow precipitates, the grains are loose and can easily slide along their neighbours' boundaries. During the process, the grains get closer, and the firn densifies. However, the more the grains are squeezed, the harder it is for them to glide. As a consequence, sliding ceases at densities around $550\,\mathrm{kg\,m^{-3}}$, where the densest packing of perfect spheres is attained (Cuffey and Paterson, 2010). Beyond this *critical point*, the densification rate decreases notably.

Over the second stage, the firn column further densifies by pressure sintering, a process during which the distance between the centre of neighbouring grains is reduced (Lundin et al., 2017). More precisely, the material is transferred to the point of contact between grains, and necks are formed between them (Cuffey and Paterson, 2010). This relocation of material takes place through sintering mechanisms, but only some of them add to the densification. Given this, Maeno and Ebinuma (1983) and Wilkinson (1988) analyzed the contribution of several sintering mechanisms to the densification of firn in polar glaciers and ice sheets and concluded that it is mainly caused by dislocation creep.

The third stage enters upon at densities around $830\,\mathrm{kg\,m^{-3}}$ when the BCO depth is reached (Cuffey and Paterson, 2010). At this point, the atmospheric air is sealed in the ice, and the firn-ice transition occurs (Schwander, 1984). Additional densification of the bubbly ice is only achieved by the slow compression of the air bubbles owing to the pressure increase, and it may be substantially affected by the flow of the ice (Salamatin et al., 1997).

This classification based on the principal mechanisms may give an impression of clear boundaries between the different densification zones. However, transitions are usually not as clearly discerned in *in-situ* density data because the change of the dominant mechanism seems to be smoother. For example, Alley (1987) argues that his model is unable to give satisfactory results around the $550\,\mathrm{kg\,m^{-3}}$ limit because the other mechanisms still play a role. Apart from that, additional critical points may exist, such as the one pointed by Maeno and Ebinuma (1983) around $730\,\mathrm{kg\,m^{-3}}$, which is usually not considered since it is even harder to spot.

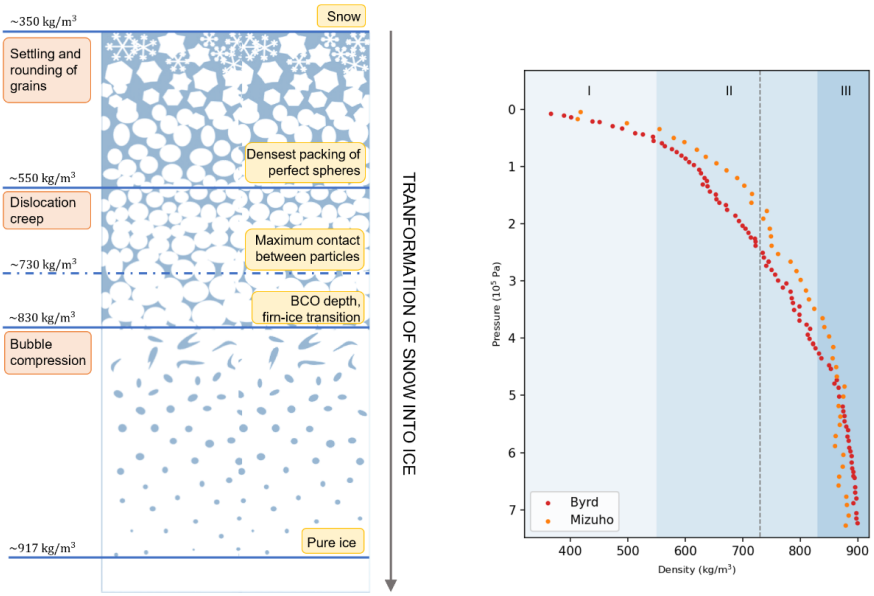

Figure 2.1: Left: Schematic representation of the transformation of snow into ice. Three stages are identified based on the principal densification mechanisms (red squares). An additional critical point was proposed by Maeno and Ebinuma (1983), but it is sometimes hard to identify (dashed line). The transitions are related to grain arrangement and air trapping (yellow squares). Modified from Blunier and Schwander (2000). **Right: Firn density profiles from two Antarctic sites.** The dashed line corresponds to the possible critical point identified by Maeno and Ebinuma (1983). The densification rate varies depending on the stage, being highest in the first and slowest after the BCO depth. Modified from Maeno and Ebinuma (1983).

2.2 Factors affecting firn densification

It is general practice to assume that the density profile resulting from the firn densification is mainly affected by the surface temperature and the accumulation rate (Herron and Langway, 1980; Lundin et al., 2017). On the one hand, high accumulation rates cause faster burial of firn and higher overburden pressures that enhance the densification rate. Therefore, if temperatures were fixed, the transition would occur quicker where the accumulation is highest. On the other hand, the process is slowed down by low temperatures; should the accumulation rate be fixed, the colder the area, the older and deeper the ice would be at the firn-ice transition zone. It must also be mentioned that when temperatures are warm enough, water may percolate through the ice column, and when it refreezes, ice lenses form. Thus, firn-ice transition happens faster in wet-snow zones (where some surface melting occurs) than in dry-snow zones (where there is no melting) (Cuffey and Paterson, 2010).

However, Alley and Bentley (1988) suggested that strain softening may also play a significant role in areas with high strain rates. More precisely, they argue that during the second stage, the densification is primarily driven by dislocation creep, which increases with the square of the effective stress. This means that reducing the effective viscosity due to strong strain rates increases the effective stress, which, in turn, enhances densification. The study by Riverman et al. (2019) has supported this hypothesis. They analyzed the density profile around the Northeast Greenland Ice Stream (NEGIS), where pronounced shear margins are present. Based on a seismic survey, they found that the firn column is up to 30 meters thinner around the shear margins and concluded that it was a consequence of the strain softening (see contour map in Figure 8.2). Then, Oraschewski and Grinsted (2022) showed that the density profiles around the NEGIS could only be reproduced by introducing a correction factor accounting for the strain softening effect in the firn densification model.

2.3 Firn densification modelling

As already mentioned before, a correct chronological interpretation of the gas measurements from ice cores requires knowledge about the so-called Δage, that is, the age difference between the trapped air and the surrounding ice. Besides, the effect of firn densification on the volume change of ice sheets must be considered when estimating the mass balance from altimetry data. Since modeling the snow-ice transformation process can provide such information (BCO depth and densification rates, among others), a wide range of firn densification models has been proposed in recent decades.

Ideally, firn densification models would be derived from first principles, but the lack of a mathematical representation able to assemble all the involved mechanisms led scientists to design empirical models primarily. Herron and Langway (1980) proposed a one-dimensional empirical model of the first and second stages of firn densification that enabled the prediction of depth-density, depth-load, and depth-age profiles based only on the temperature and accumulation rate of the site. As many researchers have used this model as a basis to develop more complex models (Barnola et al., 1991; Li and Zwally, 2011), a more detailed description of it will be provided at the end of the chapter.

Although not as numerous, attempts to derive physics-based models have also been made. For example, Alley (1987) proposed a simple model for porous firn densification by grain boundary sliding. Besides, Arnaud et al. (2000) designed a model that took into account not only boundary sliding but also plastic deformation, even though it still has parameters to be tuned empirically. However, one of the few models that accounts for the effect of horizontal stresses is the one developed by Gagliardini and Meyssonnier (1997). This model has been shown to be helpful in studying the dynamics of glaciers that are composed mainly by firn (Zwinger et al., 2007; Licciulli et al., 2020), and even in analyzing the evolution of snow caves buried in firn over time (Brondex et al., 2020). Due to these features, particularly the implicit inclusion of horizontal stresses, we have decided to take the Gagliardini and Meyssonnier (1997) model as the basis of this Master's Thesis. A more thorough description of this model is available in the following chapter.

2.3.1 Herron-Langway model

The Herron-Langway model aims to model the first and second stages of firn densification to enable the prediction of depth-density, depth-load, and depth-age profiles based on the surface density, temperature, and accumulation rate of each site. As we shall see, the model is empirical because some parameters that must be tuned to *in situ* density measurements arise during the mathematical derivation.

The model assumes steady-state conditions, and it is based on the presumption that the density changes (air space changes) are proportional to the stress variations caused by the snow accumulation.

$$\frac{d\rho}{\rho_{\text{ice}} - \rho} = \alpha \rho dh \quad \Longrightarrow \quad \ln\left(\frac{\rho}{\rho_{\text{ice}} - \rho}\right) \propto h \tag{2.1}$$

where h is the depth, $\rho_{\text{ice}} = 917\,\text{kg}\,\text{m}^{-3}$ is the density of ice, and α is the proportionality constant.

This linear relationship was confirmed when analyzing the $\ln[\rho/(\rho_{\text{ice}} - \rho)]$ vs. h graphs obtained from *in-situ* density measurements from Antarctic and Greenlandic cores. Two linear segments corresponding to the first and second densification stages could be identified in these plots, being the slope of the second zone more pronounced. Based on the equation 2.1, these two slopes can be expressed as follows and will depend on the temperature and accumulation rate on the site of interest.

$$\frac{d\ln\left[\rho/(\rho_{\text{ice}} - \rho)\right]}{dh} = \begin{cases} C & \text{for} \quad \rho < 550\,\text{kg}\,\text{m}^{-3} \\ C' & \text{for} \quad 550\,\text{kg}\,\text{m}^{-3} < \rho < 800\,\text{kg}\,\text{m}^{-3} \end{cases} \tag{2.2}$$

This equation somehow relates the density (ρ) and the depth (h), so the density profile could be deduced from it. However, it must be considered that the model aims to predict density profiles based only on the accumulation rate and the temperature of the site. Therefore, some rearrangements must be made to include these dependencies explicitly in the model. First, the accumulation rate is included by introducing the relation $dh/dt = A/\rho$ into equation 2.2, where A is the accumulation rate in water-equivalent units.

$$\frac{d\rho}{dt} = \begin{cases} \frac{CA}{\rho_{\text{ice}}}(\rho_{\text{ice}} - \rho) & \text{for} \quad \rho < 550\,\text{kg}\,\text{m}^{-3} \\ \\ \frac{C'A}{\rho_{\text{ice}}}(\rho_{\text{ice}} - \rho) & \text{for} \quad 550\,\text{kg}\,\text{m}^{-3} < \rho < 800\,\text{kg}\,\text{m}^{-3} \end{cases} \tag{2.3}$$

Then, equation 2.3 is modified based on the assumption that the temperature and accumulation rate are not correlated.

$$\frac{d\rho}{dt} = \begin{cases} k_0 A^a(\rho_{\text{ice}} - \rho) & \text{for} \quad \rho < 550\,\text{kg}\,\text{m}^{-3} \\ \\ k_1 A^b(\rho_{\text{ice}} - \rho) & \text{for} \quad 550\,\text{kg}\,\text{m}^{-3} < \rho < 800\,\text{kg}\,\text{m}^{-3} \end{cases} \tag{2.4}$$

where the constants a and b depend on the densification mechanisms and k_0 and k_1 are related to temperature by the Arrhenius equation.

Once the accumulation rate and the temperature are explicitly introduced in the model, the relationship between density and depth can be recovered by exploiting the relation $dh/dt = A/\rho$ again:

$$\frac{d\rho}{dh} = \begin{cases} k_0 A^{a-1}\rho(\rho_{\text{ice}} - \rho) & \text{for} \quad \rho < 550\,\text{kg}\,\text{m}^{-3} \\ \\ k_1 A^{b-1}\rho(\rho_{\text{ice}} - \rho) & \text{for} \quad 550\,\text{kg}\,\text{m}^{-3} < \rho < 800\,\text{kg}\,\text{m}^{-3} \end{cases} \tag{2.5}$$

This differential equations can be analytically solved by imposing the boundary conditions $h = 0$ and $\rho = \rho_0$ at the surface. This way, the depth-density relation is obtained for the first and second densification stages.

$$\rho(h) = \begin{cases} \frac{\rho_{\text{ice}} Z_0}{1+Z_0} & : \quad Z_0 = \frac{\rho_0}{\rho_{\text{ice}} - \rho_0}\,\exp[\rho_{\text{ice}} k_0 h A^{a-1}] & \text{for} \quad \rho < 550\,\text{kg}\,\text{m}^{-3} \\ \\ \frac{\rho_{\text{ice}} Z_1}{1+Z_1} & : \quad Z_1 = \frac{550}{\rho_{\text{ice}} - 550}\,\exp[\rho_{\text{ice}} k_1 (h - h_{550}) A^{b-1}] & \text{for} \quad 550\,\text{kg}\,\text{m}^{-3} < \rho < 800\,\text{kg}\,\text{m}^{-3} \end{cases} \tag{2.6}$$

Having this relationship, the last step is to determine the values of the parameters a, b, k_0, and k_1. In order to find the values of a and b, the slopes of the first and second densification stages are compared for sites (1 and 2) with similar temperature but distinct accumulations (see equation 2.7), getting as a results that $a = 1.1 \pm 0.2$ and $b = 0.5 \pm 0.2$. In the model, the values are approximated to $a = 1$ and $b = 0.5$.

$$a = \frac{\ln(C_1/C_2)}{\ln(A_1/A_2)} + 1 \qquad \text{and} \qquad b = \frac{\ln(C_1'/C_2')}{\ln(A_1/A_2)} + 1 \tag{2.7}$$

Regarding k_0 and k_1, their equations were ascertained from plots of $\ln k$ against $1/T$, being T the temperature at the site.

$$k_0 = 11\,\exp\left(-\frac{10160}{RT}\right) \qquad \text{and} \qquad k_0 = 575\,\exp\left(-\frac{21400}{RT}\right) \tag{2.8}$$

where 10160 and 21400 are the effective activation energies for the two zones in units of $\text{J}\,\text{mol}^{-1}$.

3. Governing equations and rheology

This chapter will give a deeper insight into the Gagliardini and Meyssonnier (1997) firn densification model since this project has been carried out based on it. We will begin with a presentation of the governing equations that dictate the dynamics of the fluid of interest. Then, we will conclude with details about the modeling of the firn rheology. The derivation of both the governing equations and firn rheology are provided in Appendix C, together with a more qualitative description.

3.1 Governing equations

Firn densification can be approximated as a secondary creep problem in which the density ($\rho = \rho(\boldsymbol{x}, t)$) and the velocity ($\boldsymbol{u} = \boldsymbol{u}(\boldsymbol{x}, t)$) fields are coupled by the mass and momentum balance equations. More precisely, the density is determined by the conservation of mass as

$$\frac{\partial \rho}{\partial t} + \boldsymbol{\nabla} \cdot (\rho \boldsymbol{u}) = 0, \tag{3.1}$$

which is applicable to compressible fluids such as firn. Apart from this, since firn is a Stokes fluid, the velocity field is governed by the following equation:

$$\boldsymbol{\nabla} \cdot \boldsymbol{\sigma} + \rho \boldsymbol{g} = \boldsymbol{0} \tag{3.2}$$

where $\boldsymbol{\sigma}(\dot{\boldsymbol{\epsilon}})$, $\dot{\boldsymbol{\epsilon}}$, and $\boldsymbol{g}$ are the stress tensor, the strain-rate tensor, and the gravitational acceleration, respectively.

Furthermore, the problem becomes thermo-mechanically coupled when also considering the effect of the temperature field, $T = T(\boldsymbol{x}, t)$, governed by the heat equation expressed as follows

$$\rho c \left(\frac{\partial T}{\partial t} + \boldsymbol{u} \cdot \boldsymbol{\nabla} T \right) = \boldsymbol{\nabla} \cdot (k_{\mathrm{T}} \boldsymbol{\nabla} T) + \boldsymbol{\sigma} : \dot{\boldsymbol{\epsilon}}, \tag{3.3}$$

where $c = c(T)$ and $k_{\mathrm{T}} = k_{\mathrm{T}}(\rho, T)$ are the heat capacity and thermal conductivity of ice. Here, the left-hand side corresponds to the total temporal derivative of the temperature field, which describes how $T = T(\boldsymbol{x}, t)$ varies in time taking into account the advection of the fluid of interest. The first term in the right-hand side characterizes the heat flux in and out the fluid, while the second is the heat source due to the viscous energy dissipation.

Finally, the ice sheet's surface evolution is governed by the free-surface equation, which is derived by imposing the kinematic free surface boundary condition:

$$\frac{\partial h}{\partial t} = w_{\mathrm{s}} - u_{\mathrm{s}} \frac{\partial h}{\partial x} - v_{\mathrm{s}} \frac{\partial h}{\partial y} + \dot{b} \tag{3.4}$$

where $h = h(\boldsymbol{x}, t)$ is the height of the surface, $\boldsymbol{u}_{\mathrm{s}} = (u_{\mathrm{s}}, v_{\mathrm{s}}, w_{\mathrm{s}})$ corresponds to the surface velocity and $\dot{b} = \dot{b}(\boldsymbol{x}, t)$ accounts for the surface mass balance.

Finally, it must be mentioned that even though these equations neglect the effects from primary creep, snow metamorphism, and the brittle fracturing of snow, recent studies have shown the model to help analyze firn dynamics (Zwinger et al., 2007; Licciulli et al., 2020; Brondex et al., 2020).

3.2 Rheology

The governing equations presented above describe the Stokes flow of fluids under the applied stress $\boldsymbol{\sigma}$. Therefore, to describe firn dynamics, the rheology (stress–strain-rate relationship) of firn must be introduced. In this project, the flow law proposed by Gagliardini and Meyssonnier (1997) is used, which describes firn as a non-linear viscous material that conforms with Glen's law in the limit of density approaching that of ice. Even though this rheology was initially proposed by Duva and Crow (1994) for general porous compressible fluids, it has been adopted several times for modeling firn densification (Gagliardini and Meyssonnier, 1997; Zwinger et al., 2007; Licciulli et al., 2020; Brondex et al., 2020).

The inverse rheology is derived based on the assumption that, during the secondary creep, the relation between the applied stress and the resulting deformation is given by a power law known as Norton-Bailey creep potential. Specifically, the rheology is an extension of Glen's flow law that depends on the first invariant of the strain-rate tensor, $\mathrm{tr}(\dot{\boldsymbol{\epsilon}})$, in addition to the usual second invariant, $\dot{\boldsymbol{\epsilon}} : \dot{\boldsymbol{\epsilon}}$ (see Appendix B for the detailed derivation).

$$\boldsymbol{\sigma}(\dot{\boldsymbol{\epsilon}}) = \frac{3}{4}^{(1-n)/2n} A^{-1/n} \dot{\epsilon}_{\mathrm{E}}^{(1-n)/n} \left[\frac{1}{a} \left(\dot{\boldsymbol{\epsilon}} - \frac{\mathrm{tr}(\dot{\boldsymbol{\epsilon}})}{3} \mathbb{1} \right) + \frac{3}{2b} \mathrm{tr}(\dot{\boldsymbol{\epsilon}}) \mathbb{1} \right] \tag{3.5}$$

$$\dot{\epsilon}_{\mathrm{E}}^2 = \frac{2}{3a} \left(\dot{\boldsymbol{\epsilon}} : \dot{\boldsymbol{\epsilon}} - \frac{\mathrm{tr}(\dot{\boldsymbol{\epsilon}})^2}{3} \right) + \frac{1}{b} \mathrm{tr}(\dot{\boldsymbol{\epsilon}})^2 \tag{3.6}$$

where A is the flow-rate factor that follows an Arrhenius-type activation equation: $A = A_0 \exp(-Q/RT)$, being $A_0 = 3.985 \times 10^{-13}\,\mathrm{s}^{-1}\,\mathrm{Pa}^{-3}$ the pre-exponential factor, $Q = 60 \times 10^3\,\mathrm{J\,mol}^{-1}$ the activation energy for creep, and $R = 8.314\,\mathrm{J\,mol}^{-1}\,\mathrm{K}^{-1}$ is the universal gas constant (canonical values, following Zwinger et al. (2007)). Besides, n is the flow rate factor and in glaciology is usually considered to be $n = 3$ (Cuffey and Paterson, 2010).

a and b are coefficient functions that only depend on the relative density, $\hat{\rho}$, as shown in equations 3.8 and 3.9. For high relative densities ($\hat{\rho} > 0.81$) the analytic solution presented by Duva and Crow (1994) for general porous material with flow rate n is adopted. However, the scaling law proposed by Gagliardini and Meyssonnier (1997), which was later revisited by Zwinger et al. (2007) and Gagliardini (2012), is used for lower densities. Here, it is important to note how, when the density reaches that of ice, $\rho \to \rho_{\mathrm{ice}}$, $a \to 1$ and $\mathrm{tr}(\dot{\boldsymbol{\epsilon}}) = 0$, so the Glen's flow law is recovered:

$$\boldsymbol{\sigma} = A^{-1/n} \epsilon_{\mathrm{E}}^{(1-n)/n} \dot{\boldsymbol{\epsilon}} \qquad \text{where} \qquad \dot{\epsilon}_{\mathrm{E}}^2 = \frac{1}{2} \dot{\boldsymbol{\epsilon}} : \dot{\boldsymbol{\epsilon}} \tag{3.7}$$

The values of the free parameters, $C_1 = 13.22240$, $C_2 = -15.78652$, $C_3 = 15.09371$, and $C_4 = -20.46489$, were tuned by fitting cold room experiments to the a and b values inverted from *in-situ* density measurements from the Greenlandic ice core Site-2. Even though these values of the parameters have been widely used to study firn dynamics in different scenarios (Gilbert et al., 2014; Licciulli et al., 2020; Brondex et al., 2020), it should ideally be recalibrated for each case (Brondex et al., 2020).

$$a(\hat{\rho}) = \begin{cases} a_1 = e^{C_1 - C_2 \hat{\rho}} & \text{for} \quad 0.4 < \hat{\rho} \leq 0.81 \\ a_0 = \frac{1+2(1-\hat{\rho})/3}{\hat{\rho}^{2n/(n+1)}} & \text{for} \quad 0.81 < \hat{\rho} \leq 1 \end{cases} \tag{3.8}$$

$$b(\hat{\rho}) = \begin{cases} b_1 = e^{C_3 - C_4 \hat{\rho}} & \text{for} \quad 0.4 < \hat{\rho} \leq 0.81 \\ b_0 = \left[\frac{3(1-\hat{\rho})^{1/n}}{4n[1-(1-\hat{\rho})^{1/n}]} \right]^{\frac{2n}{n+1}} & \text{for} \quad 0.81 < \hat{\rho} \leq 1 \end{cases} \tag{3.9}$$

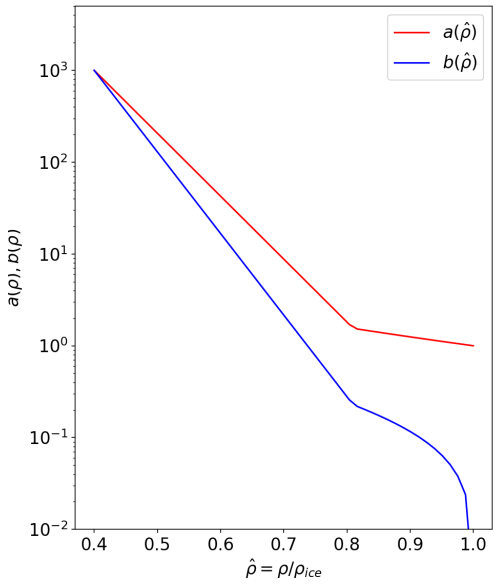

Figure 3.1: Functions a and b for different relative densities. Note that the linear section corresponds to the logarithmic scaling of the empirical part of the solution. Note that in the limit of density of ice, $\hat{\rho} \to 1$, $a \to 1$, and $b \to 0$, so the Glen's law for incompressible ice is recovered.

4. Finite Element Method

The governing equations presented in the previous chapter have been solved based on the Finite Element Method (FEM) in this project. Thus, this chapter will be devoted to giving a brief introduction to this numerical method. It will start with a short motivation, highlighting its usefulness and applications. Later, a simple example of the mathematical formulation of FEM will be provided. To conclude, `FEniCS`, the python library used to implement FEM in this project, will be introduced.

4.1 Motivation for FEM

Most physical phenomena can be described by partial differential equations, but these are analytically solvable in only a few idealized cases. Therefore, in order to solve them in more complex and realistic scenarios, the use of numerical tools is required. The FEM-based models have a great variety of applications and have become fundamental in many fields. For example, engineers adopt them to perform stress and thermal analyses of industrial parts or buildings (Fish and Belytschko, 2007), while in biomechanics, they are used to model joints and prosthetics (Marqués et al., 2022). In this work, the firn densification process is studied using the FEM.

The basis of the FEM is to split the analyzed body into little elements, usually called finite elements, that are linked to each other by nodes. The structure obtained this way is called mesh, and it can be easily designed to represent any kind of geometric domain. This is one feature that makes the FEM attractive and the main reason to use it in this project since irregular domains are hard to implement in the more common finite-difference-like methods. When solving the partial differential equations with the FEM, the value of the variable of interest is obtained for each node, which is then interpolated in space. As it is usual in this kind of method, the finer the grid, the higher the accuracy of the solution. However, since calculation time increases with an increasing number of nodes, the computational cost must also be borne in mind, and thus, a compromise between these two must be achieved.

4.2 Mathematical formulation example: 1D heat equation

Two of the main methods to solve partial differential equations are the finite-difference method and the FEM. In the former, an equation approximation is made, while the solution itself is approximated in the latter. This approximation can be best understood through a case study, which in this case will be the 1D heat equation.

The temperature field in a solid, $T(\boldsymbol{x}, t)$, evolves by heat conduction and is defined by temperature gradients and heat sinks or sources, as shown in the left-hand side of equation 4.1. In the case of a solid rod in steady state with constant thermal conductivity, the heat equation is significantly simplified, as shown in the right-hand side of equation 4.1.

$$\rho c \frac{\partial T}{\partial t} = -\boldsymbol{\nabla} \cdot (k_{\mathrm{T}} \boldsymbol{\nabla} T) + s \qquad \Longrightarrow \qquad k_{\mathrm{T}} \frac{\partial^2 T}{\partial x^2} = -s(x) \tag{4.1}$$

where ρ, c, and k_{T} are the density, the heat capacity, and the thermal conductivity of the material, respectively, and s is the heat source/sink term.

In the FEM the solution, $T(x)$, is approximated by using a set of linearly independent basis functions $\phi_i(x)$, as expressed in equation 4.2. When this approximation is introduced in equation 4.1, the problem of interest becomes under-determined since there are N unknowns (c_i) and only one equation.

$$T(x) = \sum_{i=1}^{N} c_i \phi_i(x) \qquad \Longrightarrow \qquad k_T \frac{d^2}{dx^2}\left(\sum_{n=1}^{N} c_i \phi_i(x)\right) = -s(x) \tag{4.2}$$

This issue can be overcome by using the weighted-residual method, which enables the construction of as many equations as are needed to fully define the problem. The basis of this method is that, as the solution is just an approximation, the equation is not perfectly solved, and a residual exists; the bigger the difference between both sides of the equation, the bigger the error made when introducing the approximation. The weighted-residual method states that the integrals of the residual over the entire domain vanish when weighted by a set of weight-functions w_j, as shown in equation 4.3.

$$R[T(x)] = k_{\mathrm{T}} \frac{d^2}{dx^2}\left(\sum_{n=1}^{N} c_i \phi_i(x)\right) + s(x) \qquad \longrightarrow \qquad \int_0^L w_j R[T(x)] dx = 0 \tag{4.3}$$

Then, if N non-zero, linearly independent, and integrable weight functions are prescribed, all c_is, i.e., the solution, can be determined by solving the $N \times N$ linear problem. There are different ways of defining the weight functions, and in this project, the Galerkin method will be used, where it is considered that the weight functions are the basis functions ϕ_i used to approximate the solution.

$$\int_0^L \phi_j(x) R[T(x)] dx = 0 \quad \text{for} \quad j = 1, 2, ..., N \qquad \text{where} \qquad T(x) = \sum_{i=1}^{N} c_i \phi_i(x) \qquad \Longrightarrow$$

$$\Longrightarrow \qquad k_{\mathrm{T}} \int_0^L w_j(x) \sum_{i=1}^{N} c_i \frac{d^2 \phi_i(x)}{dx^2} dx = -\int_0^L w_j \phi_j s(x) dx \qquad \text{where} \qquad w_j = \phi_j \tag{4.4}$$

Choice of basis functions

One of the principle properties of the FEM is that the equations are solved in a finite number of points, the nodes, which is a direct consequence of the choice of the basis functions. More precisely, these functions are chosen to be non-zero only between two grid points, and hence, they are finite in extent. Diverse are the functions that fulfill such characteristics, being the piecewise linear functions the simplest ones and, thus, the ones selected in this project (see Figure 4.1).

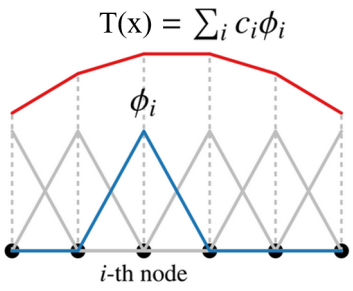

Figure 4.1: Set of linear functions that are non-vanishing only between two nodes. The solution $T(x)$ is a linear combination of these functions, and the c_i coefficients are determined by solving the $N \times N$ linear problem. Taken from Rathmann (2021).

Weak form of the equations

The second derivative of the temperature, $T(x)$, present in the linear system of equations 4.4, may cause numerical issues if the differentiability of the temperature field is limited. Also, it must be borne in mind that the second derivative of a linear function is zero and, therefore, if linear functions are chosen as basis functions, the left-hand-side term of equation 4.4 vanishes. To avoid these issues, integration by parts is applied to this particular term to reduce the order of the derivative from second to first.

$$\left[w_j(x)k_{\mathrm{T}}\sum_{i=1}^{N}c_i\frac{d\phi_i(x)}{dx}\right]_0^L - k_{\mathrm{T}}\int_0^L\frac{dw_j(x)}{dx}\sum_{i=1}^{N}c_i\frac{d\phi_i(x)}{dx}dx = -\int_0^L w_j\phi_j s(x)dx \quad \text{where} \quad w_j = \phi_j \tag{4.5}$$

Equation 4.5 is widely known as the weak or variational form due to the weaker continuity conditions required. To be more accurate, the differential equation (equation 4.1) implies that the conditions must be satisfied by the solution. In contrast, the integral equation states that those conditions only need to be accomplished in an average sense. The weak forms of the governing equations solved during this project are shown in Appendix A.

4.3 `FEniCS` Project

In this Master's Thesis project, the Python framework `FEniCS` has been used to implement the model as finite element problems. `FEniCS` is an open-source computing platform designed to solve Partial Differential Equations (PDE) based on the FEM (Alnaes et al., 2015). An especially appealing characteristic of `FEniCS` is that the user only needs to introduce the equations in the weak form and build the mesh. Then, `FEniCS` automatically approximates the solution by a linear combination of basis functions, introduces the appropriate weight functions, and solves the resulting linear problem.

Part II

Methods and Results

5. Models used during the project

During this project, we have analyzed one- and two-dimensional scenarios. More precisely, the firn rheology has been validated and recalibrated based on the 1D model, while the shape optimization and strain softening have been studied using a 2D model. Before presenting the results we have obtained, in this chapter, we will dive into the characteristics of the 1D and 2D models, such as the applied boundary conditions or the validity of several assumptions.

5.1 1D model

The non-linear thermomechanically coupled one-dimensional model consists of a column of compressible fluid. Its time evolution is dictated by the mass balance, momentum balance, and heat equations presented in the theoretical background (see equations 3.1, 3.2, 4.1), and assuming the canonical flow exponent to be $n = 3$. Starting from an initial guess of the density profile, these equations are solved subject to the boundary conditions shown in equations 5.1, 5.2, and 5.3 until steady state is reached.

$$\rho(z = 0) = \rho_\mathrm{s} \tag{5.1}$$

$$u_z(z = 0) = -\dot{a} \qquad \text{and} \qquad u_z(z = -H) = -\dot{a}\frac{\rho_\mathrm{s}}{\rho_\mathrm{ice}} \tag{5.2}$$

$$T(z = 0) = T_\mathrm{s} \qquad \text{and} \qquad \frac{\partial T}{\partial z}(z = -H) = q \tag{5.3}$$

where ρ_s, $\dot{a}$, and T_s are the surface density, accumulation rate, and temperature measured at each site. H is the height of the firn column, and q refers to the heat flux at the bottom of the column.

Equation 5.2 implies that the mass fluxes into and out of the firn column are equal, but it is only fulfilled if the firn column is deep enough to ensure there is pure ice at the bottom. Therefore, we have set the initial height to be $H_\mathrm{init} = 180\,\mathrm{m}$ at every site. However, the height of the column must be updated at each time step based on the velocity at the bottom and the accumulation rate.

$$H_{n+1} = H_n + \Delta H = H_n + [u_z(z = -H) + \dot{a}] \cdot \Delta t \tag{5.4}$$

where n and $n + 1$ stand for the previous and following time steps, respectively. This change in height is important since it defines whether the column has reached steady state. Specifically, we have decided that steady state is reached when $\Delta H/\Delta t < 0.01\,\mathrm{m\ yr^{-1}}$.

Regarding the rheology, due to numerical stability reasons, the coefficient functions a and b (see equations 3.8 and 3.9) have been modified as

$$a = a_0 + \mu\ a_1 \qquad \text{and} \qquad b = b_0 + \mu\ b_1 \qquad \textit{where} \qquad \mu = \frac{1}{1 + \exp[-\gamma_\mu(\hat{\rho}_\mathrm{c} - \hat{\rho})]} \tag{5.5}$$

where μ is the logistic function that smoothens the transition, and γ_μ is the parameter that controls the level of smoothness, here taken to be $\gamma_\mu = 20$. This way, we achieve a smooth transition between the scaling law (a_1 and b_1) and the theory based expression (a_0 and b_0) (see Appendix B for a detailed explanation). In addition, we have reduced the number of parameters from four (C_1, C_2, C_3, and C_4) to one (K). To do so, we have imposed the continuity of the functions a and b and exploited the fact that the energy dissipation must always be positive (further details are provided in Appendix B).

Finally, it is important to note that the coefficient function b goes to 0 as we approach the density of pure ice, which translates into an asymptote in our equations. This implies that the density, ρ, must not exceed this value, but it can not be ensured in our numerical scheme. In this project, we have simply *clamped* the density, i.e., whenever the density at a point exceeds $0.99 \cdot \rho_{\text{ice}}$, we set it back to $910\,\text{kg}\,\text{m}^{-3}$. Even though this approach is good enough for our purposes, there are more elegant ways of handling this issue, such as automatically switching to an incompressible flow regime or changing to a more stable set of coordinates.

Weak thermal coupling and steady state assumptions

This thermomechanically coupled firn densification model may be simplified in some cases. On the one hand, even though there is a seasonal variation in the uppermost 10 meters, the temperature is usually almost constant through the firn column in Greenland (see left-hand side of Figure 5.1). Consequently, the temperature can be considered depth-constant and no longer involved in the problem. On the other hand, in scenarios where the accumulation rate, the temperature, and the surface density remain nearly constant, the steady state assumption can be made. If both conditions are assumed, the problem is reduced as shown in equation 5.6, where the boundary conditions 5.1 and 5.2 apply. For example, we can see how GRIP is a site where the weak thermal coupling and the steady state assumptions are adequate since the resulting density profiles do not differ much from each other (see right-hand side of Figure 5.1).

$$\boldsymbol{\nabla} \cdot (\rho \boldsymbol{u}) = 0 \qquad \text{and} \qquad \boldsymbol{\nabla} \cdot \boldsymbol{\sigma} + \rho \boldsymbol{g} = \boldsymbol{0} \tag{5.6}$$

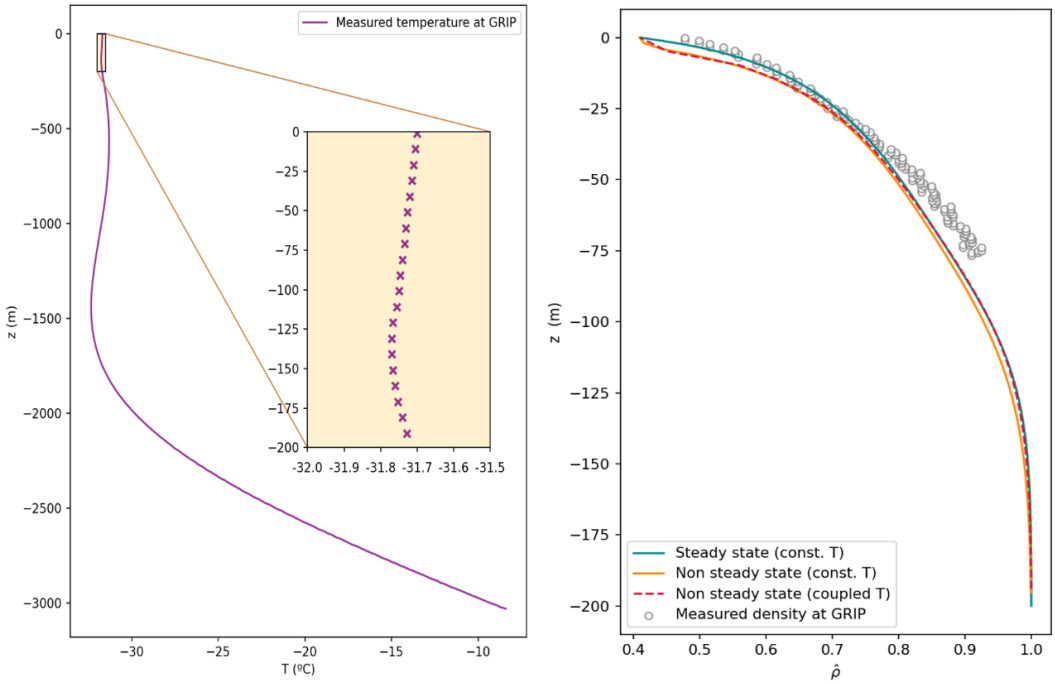

Figure 5.1: Left: Temperature profile from GRIP ice core (Johnsen, 2003). The temperature is almost constant at the first 200 m of the ice column. The temperature increase in the last 1000 m is caused by the geothermal heat flux. **Right: Comparison of density profiles with different assumptions.** The steady state and the weak thermal coupling assumptions have little impact on the final density profile. The grey dots represent the *in situ* density measurements from GRIP. The model has been run based on the measured accumulation rate and the temperature at GRIP, which have been kept constant throughout the simulation.

5.2 2D model

The one-dimensional model can be extended to two dimensions just by handling the new lateral boundaries. Specifically, the horizontal velocities have been set to zero so that there is no horizontal mass flux out of the firn column. The rest of the boundary conditions and the governing equations remain the same. The horizontally uniform density profile we obtain from this model is identical to the unidimensional solution.

However, in the shape optimization and the strain softening problems we will present later, the horizontal symmetry of the velocity field is lost. Therefore, the surface evolution can not be implemented as uniform anymore. In these cases, the displacement of each surface point will be different and, thus, has to be calculated. In order to do so, we will use the surface evolution equation introduced in Chapter 3 (see equation 3.4). The surface heights are calculated after every timestep, and a new mesh is created accordingly.

When analyzing the temporal evolution of a tunnel, though, there is an extra surface to take care of. Despite the fact that the inner surface of the hole is also stress-free, the aforementioned method can not be applied because equation 3.4 can not deal with closed loops. As an alternative, we have used the built-in function `ALE.move()` from `FEniCS` that, in our case, displaces the nodes according to the displacement function $\boldsymbol{u}\ dt$. This method can not account for the accumulation at the surface, but this is not a problem since the simulated time periods will be short in the shape optimization problem (5-10 years).

The drawback of `ALE.move()` is that, as the nodes are displaced, mesh defects accumulate; in some cases, the local node density becomes too high, while the cells overlap in others. However, this issue can be overcome by rebuilding the mesh periodically (every third timestep in our case). We have used the `gmsh` library to remesh these irregular meshes since, after the first time step, we can not describe them with `FEniCS`' basic geometrical functions anymore (Geuzaine and Remacle, 2009).

6. Validation and recalibration

The first aim of the project is to validate the Gagliardini and Meyssonnier (1997) model by trying to recreate the density profiles from six Greenlandic ice cores: Site-2, Site-A Crête, DYE-3, GRIP, NGRIP, and NEEM. More precisely, we will assess the model's validity by comparing the inverted temperatures to the *in situ* temperature measurements of each site. Then, we will try to recalibrate the model by comparing the model's performance for different values of the K parameter.

6.1 Validation of the rheology

Models must be validated based on verified data before applying them to complex and unknown scenarios. In this case, the model's performance could be assessed by comparing the modeled density profiles to the *in situ* depth-density measurements. However, we know beforehand that the model will not be able to reproduce all the characteristics of the measured profile because it does not account for all the mechanisms behind densification. So, beyond saying whether the results and measurements are closer or further away, it is hard to determine the adequacy of the results. Thus, to overcome this issue, we have evaluated the model based on how correlated the model-inferred temperatures are to those measured in the field.

With this aim, we have reproduced the density profiles from six Greenlandic ice cores (Site-2, Site-A Crête, DYE-3, GRIP, NGRIP, and NEEM) for four different values of the *compound parameter*, $K = \{10, 100, 1000, 10000\}$. To do so, we have used the 1D model based on the weak thermal coupling and steady-state assumptions, forced with the field data shown in Table 6.1. After modeling the density profile, we have fitted it to the observed data, leaving the depth-constant flow rate factor, $\bar{A}$, as the free parameter. Once the best fit, $\bar{A}$, is known, computing the modeled temperatures is straightforward because $\bar{A}$ follows an Arrhenius-type activation equation, $\bar{A}(\bar{T}) = A_0 \exp(-Q/R\bar{T})$.

We have obtained the best fit $\bar{A}$ by a *Newton conjugate gradient descent* of the model-data misfit functional

$$J(\bar{A}) = \int_{-H}^{0} \left|\rho(z;\bar{A}) - \rho_{\text{obs}}(z)\right|^2 dz. \tag{6.1}$$

The gradient of J has been evaluated using the adjoint-based optimization method implemented in `dolfin-adjoint` (Mitusch et al., 2019), a library that allows to derive and solve the adjoint equation automatically for each gradient evaluation given a forward model in the finite element software `FEniCS` (see Appendix C for further information).

Table 6.1: Depth averaged temperature and accumulation rate of each site used to force the model. Accumulation rate data for all sites have been retrieved from Bréant et al. (2017). *We have used the surface temperature instead due to the lack of the temperature profile.

Site	Depth averaged temperature (°C)		Accumulation rate (w.eq., myr^{-1})
Site-2	−25.0 *	(Langway, 1967)	0.360
Site-A Crête	−29.5	(Clausen et al., 1988)	0.282
DYE-3	−21.0	(Dahl-Jensen et al., 1998)	0.500
GRIP	−31.7	(Johnsen, 2003)	0.210
NGRIP	−31.5	(Dahl-Jensen et al., 2003)	0.175
NEEM	−28.8	(Orsi et al., 2017)	0.200

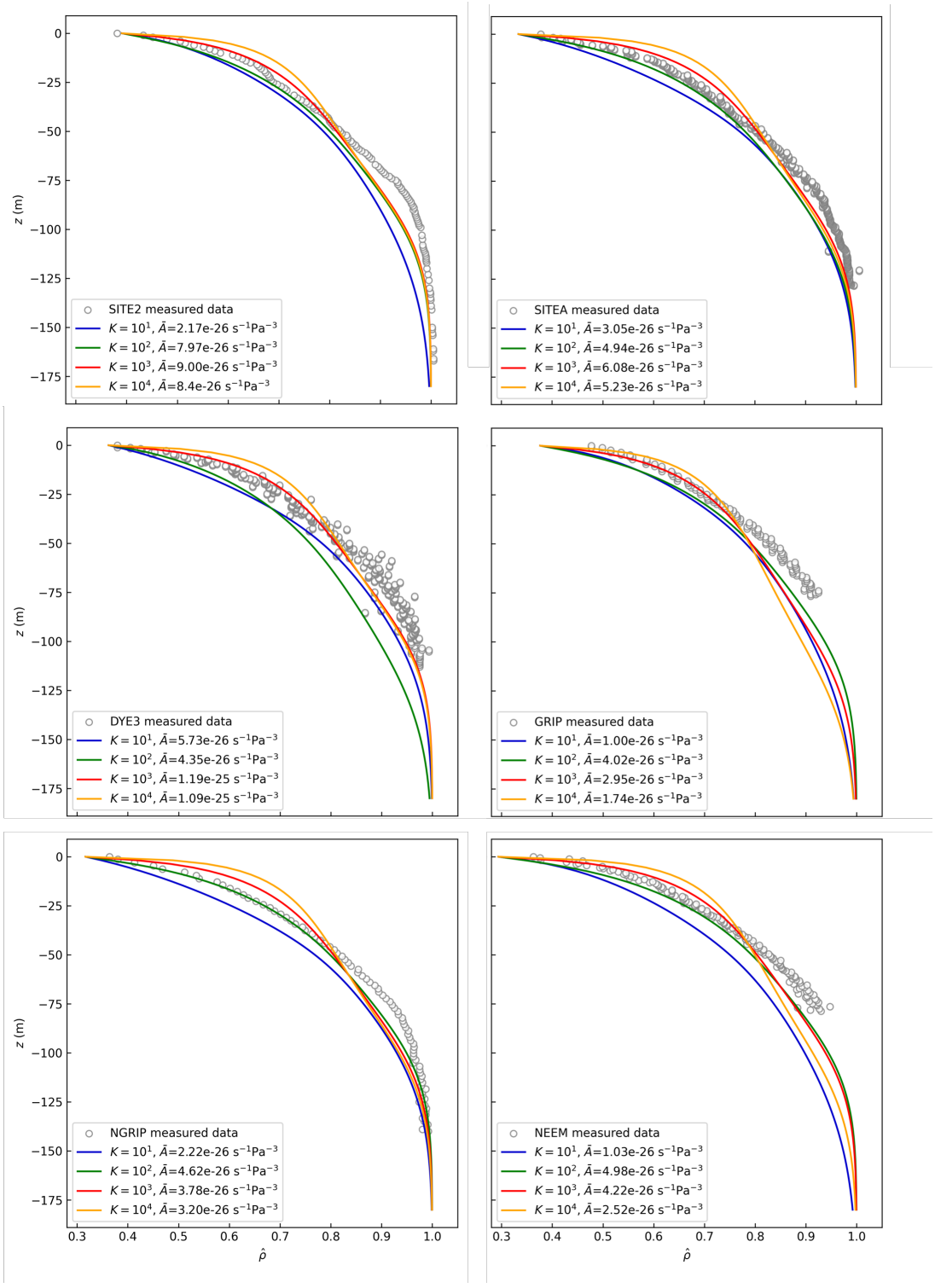

Figure 6.1: Values of the best-fit ($\bar{A}$) and their corresponding modeled density profiles for K ={10, 100, 1000, and 10000} at each of the analyzed sites. The dots represent the *in situ* density-depth measurements retrieved from Bréant et al. (2017). The influence of K in the resulting profile is most evident in the first 20-30 meters; the higher the value of K, the higher the densification rate. Apart from this, the model generally struggles to reproduce the densities for $\hat{\rho} > 0.8$, where the predicted densification rates are too low for all Ks. Note that, although there are some slight collapse rate increases in the data, the apparent *bump* is just a perception issue pronounced by all the curves suddenly failing to follow the trend.

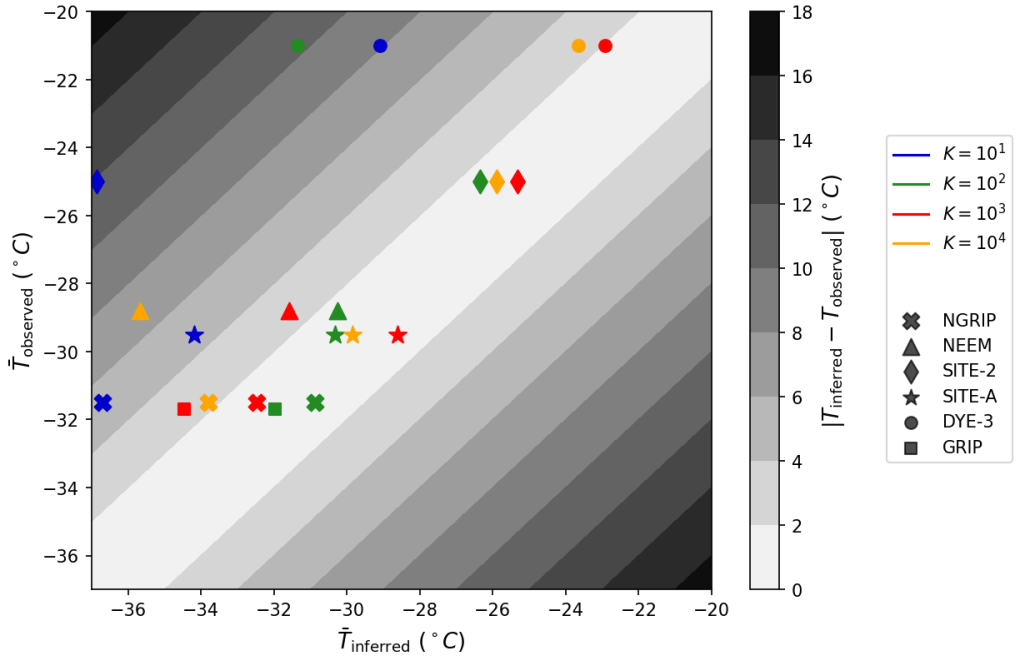

Figure 6.2: Scatter plot showing the relationship between inferred and observed temperatures for K ={10, 100, 1000, and 10000} at each analyzed site. The color gradient behind represents the distance between the observed and inverted temperatures. The model's performance depends on the value of K; the model with $K = 10$ clearly fails to estimate the measured temperatures, while it is unclear which of the higher Ks gives the best overall results.

The results of this analysis are shown in Figures 6.1 and 6.2. Figure 6.1 shows the modeled density profiles of each analyzed site for the four values of the best fit, $\bar{A}$, obtained in the fitting. A quick look is enough to identify some general trends present in the profiles of every site for all the Ks. First of all, the parameter K strongly influences the densification rates of the first ~ 25 meters; the higher the value of K, the faster the densification process. Apart from this, the results are not very satisfactory for relative densities higher than 0.8, where all the predicted densification rates are too low. However, in most cases, the model still seems to be relatively successful at predicting the depth of transition to pure ice.

If we look at the model's performance for each specific K, it is evident that $K = 10$ cannot reproduce the density profiles of any of the sites. Apart from this, despite being slightly better, the results for $K = 10^4$ could be better, too, since the predicted densification rates are too high for the first meters. The performance of $K = 10^2$ and $K = 10^3$ is variable and depends on the site, but we can see how, for $\hat{\rho} < 0.8$, the measurements' data points always fall in between these two lines.

In the same line, we can see how the inverted temperatures shown in Figure 6.2 support the idea that, with $K = 10$, we fail to model the densification rates (all the inferred temperatures are more than 4°C away from the measured values). Similarly, with $K = 10^4$, the results are closer to the observations, but the spread is still huge (note that the GRIP point lays out of the frame). Nevertheless, it is not straightforward to assess which of the other two values gives the best overall results because, besides the DYE-3 outlier, the distance between all the inverted and observed temperatures is reasonably small.

These results suggest that, up to a point, the model is able to reproduce the expected behavior for Ks ranging from 100 to 1000. However, this analysis is not enough to assess whether there is some value (or sweet spot) in between that might yield better results. If this were the case, we would be talking about a universal value of K. However, having seen some variability in the reaction to changing K values, we can not rule out the possibility of K being site-dependent. Therefore, the next section is devoted to analyzing these possibilities more in-depth.

6.2 Recalibration of the rheology

Until now, the studies carried out based on the Gagliardini and Meyssonnier (1997) model have relied on the values of the free parameters that were proposed when the model was published, i.e., $K = 1000$. However, we have shown in the previous section that it is not straightforward to conclude which set of parameters gives the best results. Thus, in this project, we have tried to assess whether other values of K perform better than the widely used $K = 1000$ and whether K is universal (a value applicable to all sites, no matter the local characteristics) or should be adjusted for each scenario of interest.

6.2.1 Global study of K

Until now, our analysis has implicitly assumed the existence of one single value of K applicable to all the sites. However, with only four Ks, it is difficult to spot any hypothetical, optimal value. Therefore, we have extended our analysis to cover a broader range of values (200 points between 10^2 and 10^4), and we have used the linear regression to measure their adequacy systematically. More precisely, we have performed the linear fit for each set of six points corresponding to a different K. Thus, the best global value of K would correspond to the one closest to the $y(x) = x$ curve, which has a slope of 45° and crosses the origin.

The results of this analysis are shown in Figures 6.3 and 6.4. Regarding Figure 6.3, the left-hand side is just an expansion of Figure 6.2, while the results of the linear fits are shown on the right-hand side. It seems that, at least for the cases we are analyzing, the colder the site, the more sensitive the model is to the magnitude of K. This variability in the sensitivities has the overall effect of lowering the slope as K increases, which, in turn, moves the intercept further away from zero.

These features can be seen more clearly in Figure 6.4, where the slope, intercept, and R^2 value of the fits are plotted. Neglecting the more irregular lowest values, we get the best results for Ks around 300, which have the highest R^2 and are closest to the target diagonal. However, if the related uncertainties are taken into account, this distance is not significant until $K \sim 3000$. Therefore, from the point of view of this analysis, all these sets of parameters are equivalent. Thus, at least with such a small sample size, we can not make a case for a precise best global value, but we can not rule out its existence, either.

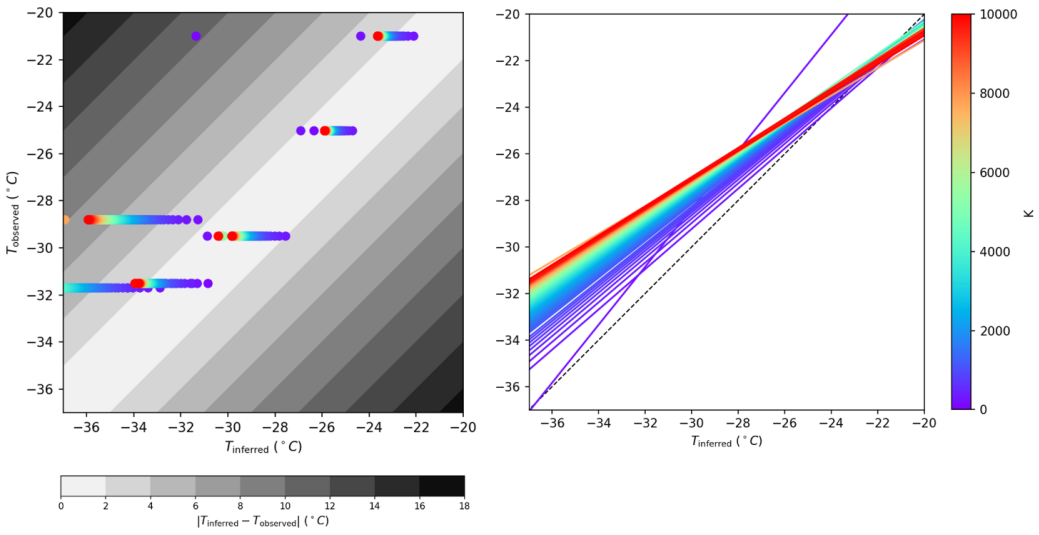

Figure 6.3: Extended scatter plot of the observed and inferred temperature and the corresponding linear fits. The scatter plot has been obtained by performing the temperature inversion presented in the previous section for a wider range of Ks. Then, each of the set of points has been fitted linearly. It seems that the coldest sites are the most sensitive to K.

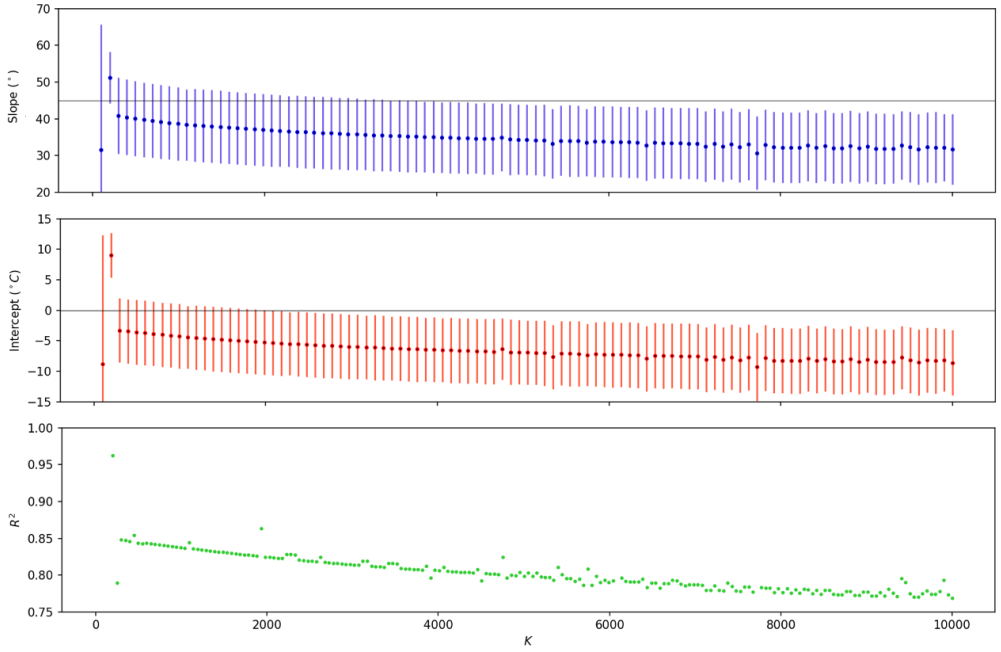

Figure 6.4: Slope, intercept, and R^2 values for each of the performed linear regressions. There is a trend to go away from the target values as K increases but, due to the big uncertainties, the results are inconclusive in the range of interest ($K \in [100,\ 3000]$).

6.2.2 Site by site study of K

Another approach to analyze the problem is to look into the local performance of each K and see if there is any agreement between them. In order to do so, instead of comparing the temperatures inverted from the output densities, we will directly compare these profiles to the measured data. More precisely, we will calculate the Root Mean Square Error (RMSE), which measures the average deviation with respect to a reference.

$$\text{RMSE}\ (\rho, \rho_{\text{obs}}) \ = \ \sqrt{\sum_{i=1}^{N} \frac{(\rho^i - \rho^i_{\text{obs}})^2}{N}} \tag{6.2}$$

where ρ^i and ρ^i_{obs} are the i^{th} element of the modeled densities ρ and the observation dataset ρ_{obs}, respectively. N corresponds to the total number of data points to be compared.

Computing this measure for each K at every site, we get the results shown in Figure 6.5. It is clear from this figure that RMSE tends to rise with increasing Ks, which means that the observed and modeled densities are distancing themselves apart. Focusing on the values between 100 and 1000, we can see that the results are highly variable until $K \sim 300$, but we can find the minimum immediately after. This behavior is shared between all the analyzed sites, and the minima seem to fall relatively close to each other. The differences in this smaller range are not very big, so we probably can not argue that we have found a precise best value. However, the sweet spot does seem closer to 300 than 1000 again, which suggests that it might be a safer guess.

Given this, it looks like the *compound parameter* might be lower than 1000 and does need to be readjusted. Unfortunately, we cannot confidently propose a new value with the assessment performed so far. Hence, we decided to conduct one last experiment.

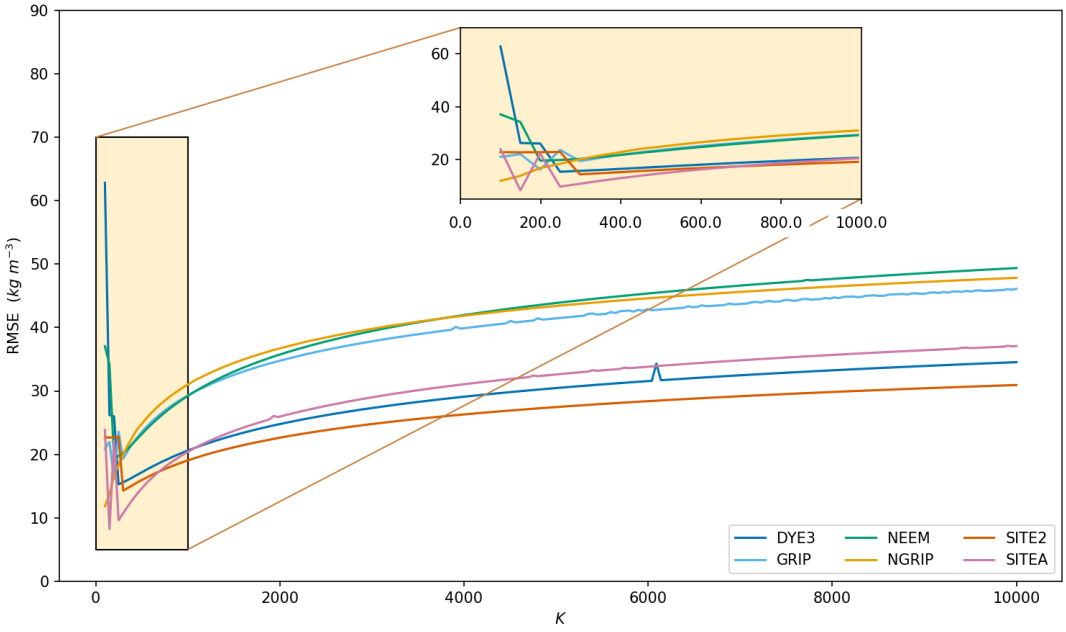

Figure 6.5: The RMSE between the best model density profiles and the actual *in situ* density measurements for each of the analyzed Ks. Leaving aside the more unstable solutions obtained for $K < 300$, all the sites follow a similar increasing trend. Moreover, there seems to be a sweet spot that would be closer to 300 than to 1000. Note that even though the RMSE is a normalized metric, the magnitude of these RMSEs can not be compared across sites. The reason is that the model is bound to eventually reach the density of ice regardless of the value of K, so the more data points we have close to the density of ice, the more biased the RMSE will be towards lower values.

6.2.3 Tunnel deformation at NEEM

In this last test, we will exploit the fact that the densification process is most sensitive to K at the first meters of the firn column. More specifically, we will model the deformation of a circular tunnel and compare it to the field experiment conducted at NEEM from 2012 to 2015. This was the first trial to construct subsurface tunnels based on the *the snow-blowing casting technique* (i.e., the *balloon method*) that we will introduce in the following chapter. In order to assess the performance of the technique, the dimensions of the hole were measured again three years after its construction.

In the following analysis, we will recreate the initial state of the experiment and model its evolution over the next three years. This study will be carried out for several values of K, and we will assess their performance by taking advantage of the aforementioned measurements. The results are summarized in Figure 6.6, where the reference dimensions are represented in red.

Once again, we can see that the lower the K, the stiffer the firn and, thus, the less the tunnel deforms. As expected, with $K = 100$, the densification rate is not high enough, while, consistent with our previous results, $K = 1000$ results in too much compaction. The best results are obtained for $K \sim 500$, which agrees well with both the reference's width and height.

Therefore, taking this into account and bearing in mind the results of the previous analyses, we have decided to consider the compound parameter to be global and with a value of 500. The assumption of globality has been shown plausible in the first two studies, while we have considered the more sensitive tunnel deformation study to determine the value.

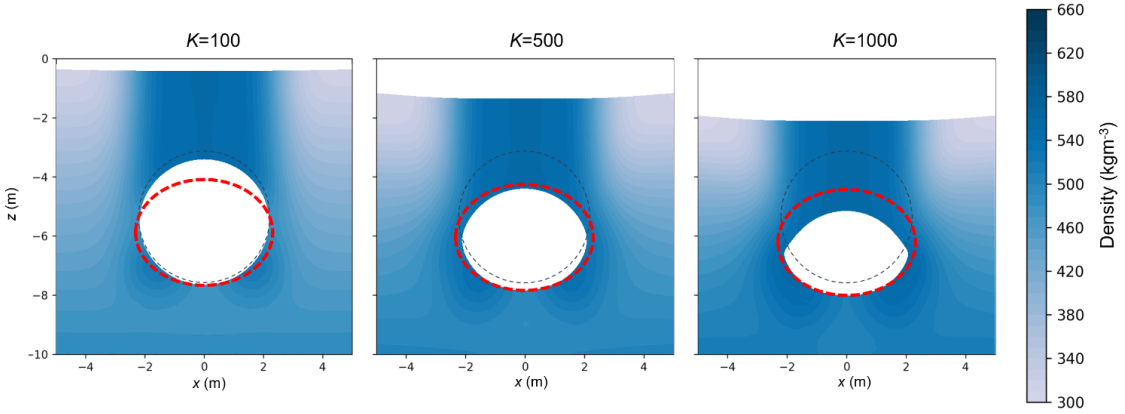

Figure 6.6: Deformation of a circular tunnel over three years. The grey dotted lines represent the initial shape of our mesh and the tunnel dug at NEEM. The red ellipse represents the final measurements used as a reference. The most satisfactory results are obtained when running the simulation with $K \sim 500$. Note that the depth of the ellipse has been adjusted for each case.

7. Shape optimization

In this chapter, we will explore the effect the initial shape of a tunnel has on its time evolution. We will first describe the importance of this problem and then try to find a shape that minimizes the collapse rate. We will briefly discuss the design of the problem and the method used to solve it, and we will finish by showing the results we have obtained.

7.1 Motivation of the problem

Tunnel deformation is a problem of great importance for the ice-core-drilling projects in Greenland and Antarctica, where usually a system of *under-ice* tunnels is dug to perform the scientific activities relatively isolated from the harsh environmental conditions. The longer these tunnels last, the better, but since the expected duration of these projects is around half a decade, they often deform too much and require maintenance to stay functional. This is a tedious and expensive task that takes a lot of time and energy from the research activities. Thus, any potential improvement is worth looking into, especially if achieved by a relatively easy-to-implement change in the initial shape of the tunnel.

We have shown in the previous chapter that this model can be applied to evolve the cross-section of a tunnel over time. In that case, the purpose of the study was to analyze the impact the magnitude of the *compound parameters*, K, had on the deformation process. However, once the value of this constant has been fixed, we can actually run the model to see how the initial shape of the tunnel affects its evolution.

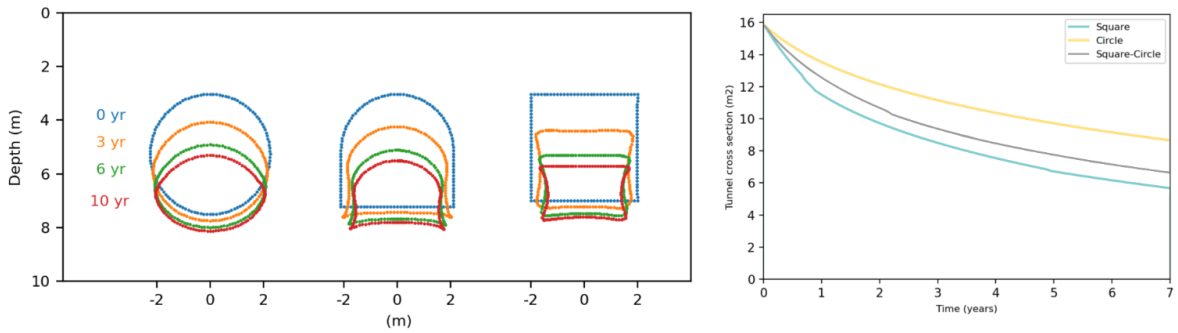

Figure 7.1: Time evolution of different initial shapes. Left: Cross-section evolution for ten years of simulation. Right: Time evolution of the *volume* of the tunnel (area of the cross-section).

As shown in Figure 7.1, the initial shape of the tunnel does indeed impact its closure. We can see how the rectangular proposal deforms the most in both the horizontal and vertical directions. The circular, instead, manages to withstand this deformation better, especially in the horizontal axis. Note that the velocity at which they deform also changes, being the rectangular the worst still. The central variant corresponds to the simplest implementation of a circular tunnel in the field. We will look deeper into the details of its construction now, but we can see how it has already lost most of the benefits of its rounder counterpart.

Apart from confirming that there are significant differences in the performance of the various proposals, these results imply the existence of some optimal shape that deforms the slowest. Figure 7.1 already hints at some of its features, but, in this chapter, we will try to find this theoretical optimum shape systematically.

7.2 Design of the problem

In order to find a proper solution that could potentially be implemented in the field, we must identify the underlying practical limitations that need to be taken into account. Some of these constraints are deeply related to how these tunnels are built, so we will briefly introduce this process. There are several ways of constructing these tunnels, but in this project, we will mainly discuss the latest (and more convenient) *balloon method*.

The main idea behind this method is to blow snow out of a trench, where a cylindrical inflatable balloon will be located. After pumping the balloon up, snow is blown back again, burying it in a more closely packed (denser) firn, $\rho_{\text{trench}} = 550\,\text{kg}\,\text{m}^{-3}$ (Brondex et al., 2020; Steffensen, 2022). Finally, after a couple of days, the balloon can be deflated and safely removed without losing the structure of the hole.

In the most straightforward implementation, the trench is as wide as the balloon, which results in a circular ceiling with a rectangular lower part (because the balloon itself *seals* those corners). In more sophisticated versions, the trench can be made broader or narrower. In the first case, the remanent width serves as a *supporting wall* that, once refilled with the denser firn, adds to the tunnel's durability. In the latter, the shape of the balloon can be modified by *squeezing* it, which translates into more egg-shaped cross-sections. There are fancier combinations of these two cases, but since we are just interested in a general characterization of the behavior, we will not look into them so far.

Another dimension of the problem is how high the trench is. The deeper the hole, the denser the firn around it, which favors its stability. However, this is usually constrained by the potency of the snow-blowers, which cannot blow the snow much higher than seven meters. This means that, in order to go deeper, auxiliary *terraces* must be dug at the sides (onto which keep blowing the snow).

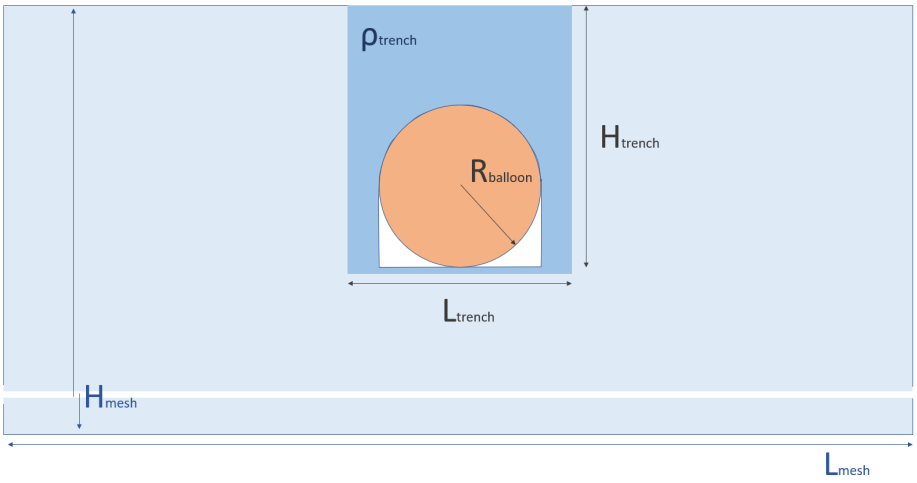

Figure 7.2: Dimensions of the tunnel. Dimensions we have taken into account in our analysis. The thickness of the supporting walls is, thus, $\Delta L = (L_{\text{trench}} - 2\ R_{\text{balloon}})/2$. The light blue area's density will follow the profile at NEEM, while the darker area corresponds to the denser snow blown on top of the balloon ($\rho_{\text{trench}} = 550\,\text{kg}\,\text{m}^{-3}$). We have set the dimensions similar to those used in EastGRIP: $R = 2.5\,\text{m}$, $H_{\text{trench}} = 8\,\text{m}$, and $L_{\text{trench}} = 5\,\text{m}$ or $L_{\text{trench}} = 7\,\text{m}$ depending on the thickness of the walls (Steffensen, 2022). H_{mesh} and L_{mesh} are big enough to make the solution independent of their value (30 and 20 meters, respectively).

Thus, as we can see in Figure 7.2, the magnitudes that will define our setup's initial conditions will be the tunnel's (l and h) and the trench's (L and H) dimensions. A circle of diameter l will initially form the upper part of the hole, and due to functionality constraints, the floor will be flat. We will also refill the $\Delta L = (L - l)/2$ wide space on both sides to assess the impact of the *supporting walls*.

Finally, on top of all this, the fuel and workforce supply in the field is limited, which adds the implicit constraint that everything should be achieved by moving the least amount of material possible. This bounds the dimensions of the problem heavily, and in order to keep the study as relevant as possible, we will deviate little from the actual magnitudes that have been implemented so far.

7.3 Definition of the optimization method

After determining the initial dimensions of the hole and how wide the supporting walls will be (if any), we can proceed to design an algorithm that computes the optimal shape. However, to do so, we must define what this optimality looks like in the first place.

It is clear that our main interest is to minimize the deformation of the hole over an average duration of a drilling project (~ 6 years). Due to the high computational cost of evolving each slight modification of the proposal, we will only compute the initial collapse rate instead. The adequacy of this simplification will be assessed in the upcoming discussion section.

However, one must be cautious when defining what is wanted from a complex optimization process like this. Only requiring the collapse rate to be minimized would make the hole go deeper into the denser (and thus more stable) firn. Likewise, since the collapse rate is integrated along the whole surface of the tunnel, there would be a bias toward reducing the perimeter instead. Finally, as previously mentioned, we want to keep the floor flat for construction and functionality reasons.

Thus, the true, complete question we are interested in answering would be:

> What is the tunnel shape that, while keeping a flat floor and the initial dimensions (width, depth, and supporting walls), minimizes the *total* (integrated) initial collapse rate without exploiting a decrease in perimeter?

Now, we only need to translate this into a mathematical formulation that we can implement.

7.3.1 Mathematical formulation of the problem

We will define the *cost function*, J, a metric of how poorly the current proposal satisfies our interests. The lower its value, the better the solution, and thus, the theoretical optimum can be found by performing a minimization analysis. This function will sum all the individual constraints, each weighed by a parameter that controls their relative importance.

Our primary term is, obviously, the instantaneous initial collapse rate. Only the normal component of the velocities at the hole's surface affects the volume change, so we will start by integrating it along the inner boundary.

$$J_{\text{collapse}} = \int_{\partial\Omega} \boldsymbol{u} \cdot \hat{\boldsymbol{n}} \, ds \tag{7.1}$$

where $\boldsymbol{u}$ is the velocity field, $\hat{\boldsymbol{n}}$ is the inwards normal unitary vector, and $\partial\Omega$ is the surface of the tunnel. In order to impose the constraints related to the hole's depth and volume, we will penalize any deviation from the initial proposal's.

$$J_{\text{vol}} \;=\; \alpha \cdot \Delta V^2 \qquad\qquad J_{\text{center}} \;=\; \beta \cdot \Delta \boldsymbol{r}_c^2 \tag{7.2}$$

where ΔV is the difference in volume and $\Delta \boldsymbol{r}_c^2$ is the distance the barycenter has been displaced. The constants α and β control the relative strength of these costs and will be defined in the following subsection. Finally, regarding the floor, it will be kept flat by restraining the movement of the lower nodes (setting as a boundary condition that their velocity should be 0).

Nonetheless, these limitations are not enough to ensure the method's stability since, with so many nodes and no impediment to overlap the mesh, quirky and unphysical solutions are still common. These artifacts always involve loops, so we will try to increase the cost of wiggly behavior by computing the laplacian of the relative position vector of the nodes (with respect to the barycenter of the tunnel). This new term will be integrated along the whole inner surface and will be bigger the more variable the *radial distances* are.

$$J_{\text{stab}} \;=\; \gamma \cdot \int_{\partial\Omega} \nabla^2 |\boldsymbol{R}_{\text{node}}|^2 \; ds \tag{7.3}$$

where $\boldsymbol{R}_{\text{node}}$ is the relative position vector with respect to the center of the hole. Thus, summing all the terms together, we can finally construct the full cost function we will implement:

$$J \;=\; J_{\text{collapse}} \;+\; J_{\text{vol}} \;+\; J_{\text{center}} \;+\; J_{\text{stab}} \;=$$

$$\int_{\partial\Omega} \boldsymbol{u} \cdot \hat{\boldsymbol{n}} \; ds \;\;+\;\; \alpha \cdot \Delta V^2 \;\;+\;\; \beta \cdot \Delta \boldsymbol{r}_c^2 \;\;+\;\; \gamma \cdot \int_{\partial\Omega} \nabla^2 |\boldsymbol{R}_{\text{node}}|^2 \; ds \tag{7.4}$$

If we were to apply this method to a broad range of initial dimensions, it would be a good idea to normalize the two boundary integrals by the length of the actual perimeter. However, since we are only performing a simple qualitative analysis of the tunnel dimensions for EastGRIP's balloon, it will not be necessary this time.

For computational advantages explained in Appendix C, this minimization will be performed by the *adjoint method* using `dolfin-adjoint` (Dokken et al., 2020), just as we did in the 1D validation problem. However, in this case, the proposals will be nudged by imposing that the hole's surface behaves as an elastic band, as implemented by Dokken (2017).

7.3.2 Tuning the parameters

All these terms we have just presented define a *cost landscape*, which can be thought of as a combination of peaks and valleys. The magnitude of these perturbations is controlled by the relative values of the regularization parameters (α, β, and γ). Thus, as our purpose is to find the minimum height in this space, it is clear that the choice of parameters will impact the solution.

Intuitively, if α or β were too big, the volume or the position of the center of mass would be fixed, respectively. If γ were too strong, there could be no oscillations in the relative vector (i.e., the surface would be a perfect circle). On the contrary, if these values are too small, the problem becomes unconstrained and unphysical solutions arise. Therefore, we need to find a compromise between freedom and restriction to ensure stability while keeping the main constraint in command of the optimization process.

As previously explained, the floor will be kept fixed throughout the minimization, so, in this case, the barycenter constraint is not useful anymore. Therefore, we can safely set β to 0, but the balance between α and γ still needs to be worked out.

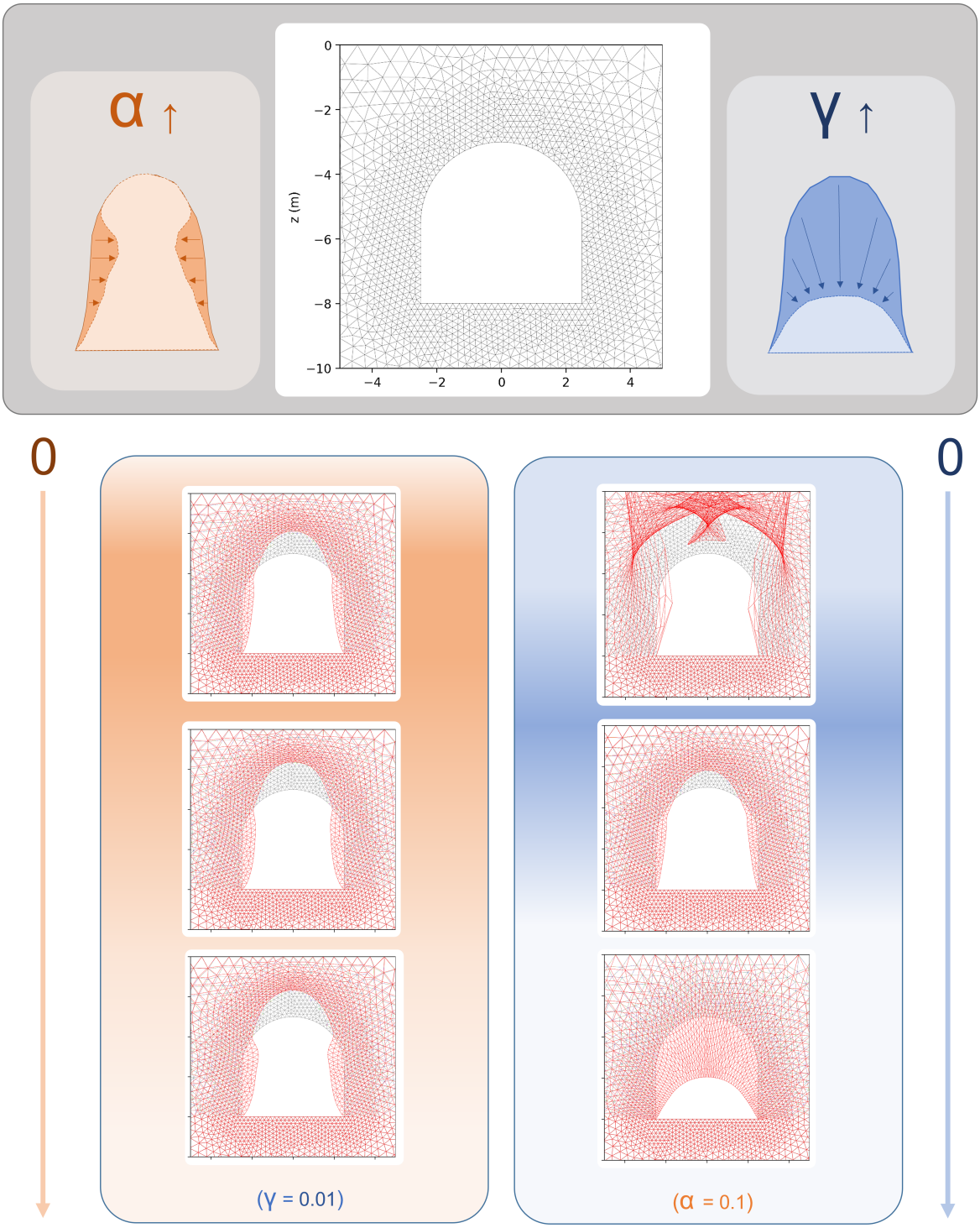

Figure 7.3: Qualitative impact of the magnitude of the parameters α and γ on the predicted optimal shape. It can be seen how the higher the values, the stronger the constraint, resulting in undesired features taking the lead (i.e., volume conservation across proposals for α and roundness for γ). The color gradient indicates the range of interest where a compromise between stabilization and constraint is met. β has been set to 0 because, having the floor fixed during the optimization process, the barycenter constraint is not required anymore.

Figure 7.3 summarizes the behavior of each regularization parameter if the rest are kept constant. As expected, increasing α forces the solution to compensate for any volume increase resulting from the main constraint, which artifactually narrows the proposal. Likewise, introducing γ regularizes the solution at first, but it quickly becomes dominant, reducing the proposal to a semicircle. Therefore, we can conclude that we are interested in the smallest non-zero value of the parameters that allow for a stable solution. Specifically, we will be using $\alpha = 0.1$ and $\gamma = 0.01$, but these values strongly depend on the mesh, so they need to be analyzed case by case for any other study.

7.4 Optimal shape and time evolution

The result of this optimization process is shown in Figure 7.4. Here we can see that, as one might have naively guessed from the start, the way to minimize the collapse rate is to form an arch-like structure. It is important to note that this particular shape has been obtained by optimizing the EGRIP-like tunnel, but we achieve the same result for any other starting mesh that shares the fixed floor's depth and length.

However, despite the careful tuning of the regularization parameters, our solution still has unwanted features that directly arise from the decision to keep our floor fixed. These artifacts are related to the fact that the optimal shape has a narrower base. Luckily, we can easily fix these by setting the floor's length to be the same as the maximum width of the arch, as shown in Figure 7.4.

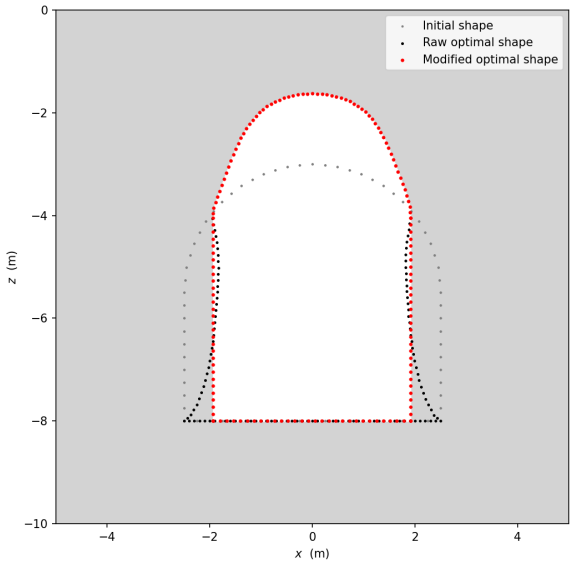

Figure 7.4: Raw and modified optimal shapes without supporting walls. The optimization process has been performed with the regularization parameter values $\alpha = 0.2$, $\beta = 0$ and $\gamma = 0.01$, and without supporting walls. We obtain this same result regardless of the initial shape (as long as they have the same floor's depth and length). The optimal shape has been modified to remove the fixed-floor-related undesired features. If we include the supporting walls, the trend is the same, but due to the denser surroundings, the optimal shape does not differ as much from the initial one.

In order to assess how this optimal shape improves the tunnel's durability, we will compare its time evolution to the default one. Figure 7.5 shows the results obtained after running the model for seven years (slightly longer than the typical duration of a drilling project). Besides, the evolution of the volume of the different shapes can be found in Figure 7.6, together with the corresponding collapse rates.

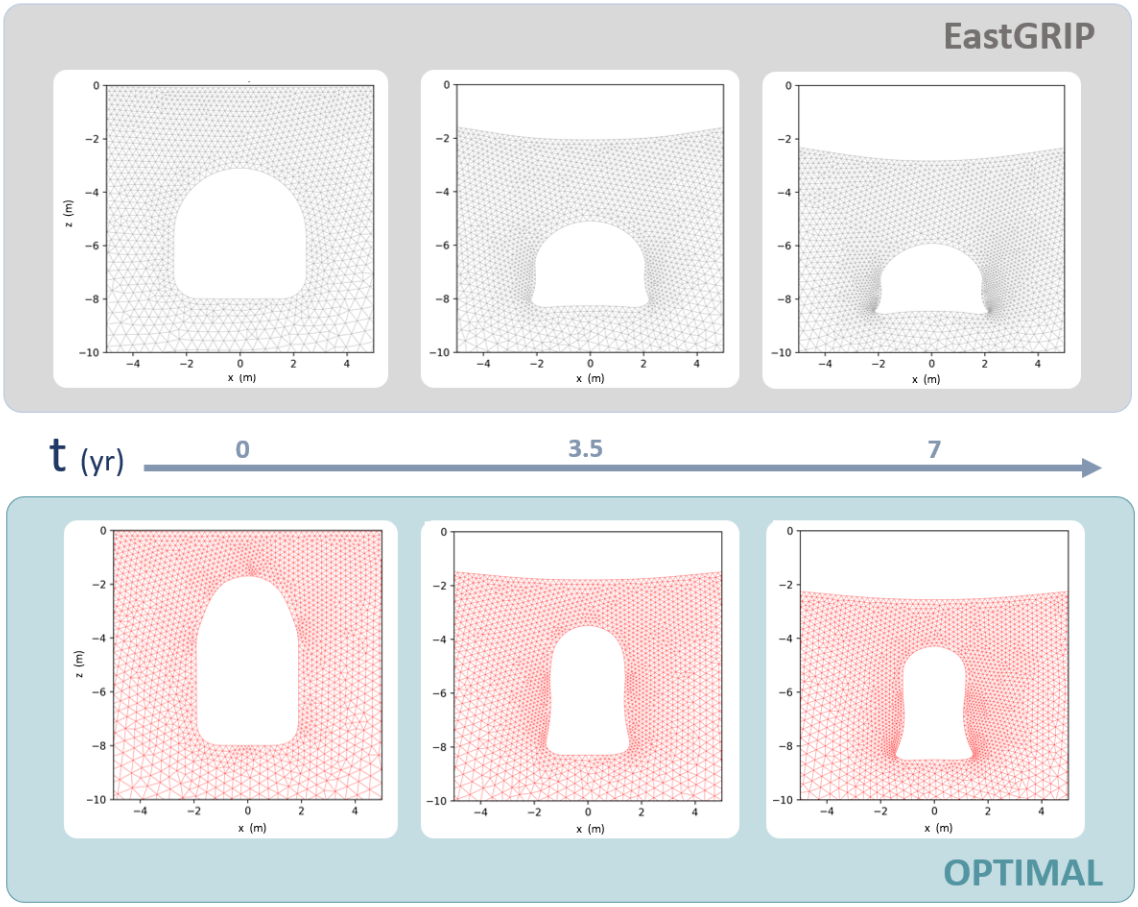

Figure 7.5: Time evolution of a tunnel similar to the ones found at EastGRIP and its optimized counterpart. Regarding the EGRIP-like shape, the width is preserved quite well, but the height loss is very pronounced. On the other hand, the optimal shape is better at conserving height, but it gets much narrower. Note that both simulations were performed without supporting walls, and lower corners were rounded to ensure numerical stability during the simulation period.

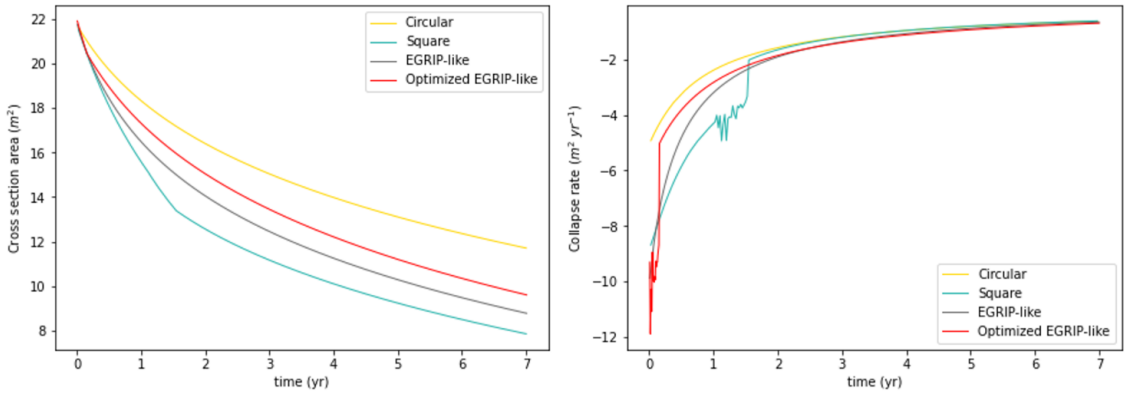

Figure 7.6: Left: Time evolution of the cross-section areas. The optimized tunnel is better at conserving the volume than the original EGRIP-like shape. The circular tunnel loses less volume than the optimal one, but they are not directly comparable due to the flat floor constraint. **Right: Collapse rate of each of the tunnels.** The initial anomalous behavior of the square's collapse rate is a result of cutting out details while remeshing.

We can see in the cross section's evolution that the optimal shape reduces the volume loss with respect to the EGRIP-like tunnel. However, as shown in Figure 7.5, this measure is far too simple to assess the improvements thoroughly. In fact, these tunnels behave quite differently; the optimal shape preserves the height at the cost of becoming narrower, while the opposite happens in the standard. This width conservation of the latter is also a feature of the circular hole (see Figure 7.1), which, at least volume-wise, still outperforms the rest. Nevertheless, not only are the scenarios not directly comparable, but there are also some irregularities in the collapse rates (product of the remeshing process). This makes the assessment harder and will be further considered in the discussion.

8. Strain softening

In this chapter, we will present the results we have obtained during the strain softening analysis, where we have tried to assess how strong horizontal stresses may affect the firn densification process. Specifically, we have introduced the horizontal strain rates from the NEGIS into the 2D model to study their effect on the BCO depth, the age of the ice at that depth, and the surface structure.

8.1 Motivation of the problem

Ice sheets' surface velocity maps are characterized by a slow-moving interior and increased velocities at outlet glaciers. However, the map of Greenland ice velocity has an added, unique ice-flow feature known as the NEGIS. This ice stream originates less than 150 kilometers from the ice divide and is the only one that extends into the interior of the ice sheet (Grinsted et al., 2022). The NEGIS was only recently revealed by virtue of satellite measurements and has been extensively studied ever since (Riverman et al., 2019; Hvidberg et al., 2020; Gerber et al., 2021; Grinsted et al., 2022).

Elevation maps obtained from ArcticDEM (Porter et al., 2018) showed that the surface follows a singular pattern at the cross-section of the NEGIS, with pronounced depressions around the shear margins (not shown in this report). Later, Hvidberg et al. (2020) verified such behavior with GPS-derived surface elevations and estimated the amplitude of the depressions to be around 20 meters. The mechanism responsible for this characteristic structure is not clear yet, but a strong candidate could be a strain softening in the zones with high strain rates, i.e., faster firn densification around the shear margins (Riverman et al., 2019; Oraschewski and Grinsted, 2022). If this were the case, the shallower BCO depth would result in a higher-than-usual gas resolution in these areas, which might make them, at least regarding this aspect, potential good spots for drilling.

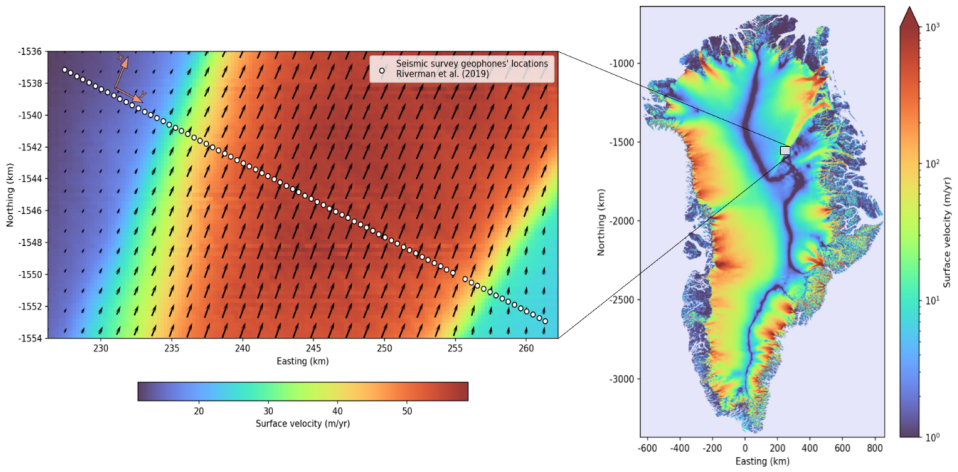

Figure 8.1: Surface ice velocity map of Greenland with a focus around the NEGIS. The map shows satellite-derived velocities from the MEAsURES program (Howat, 2020). The colormap indicates the magnitude of the velocities, while the arrows represent the direction. When focusing on the NEGIS, strong shear margins can be identified. The white dots represent the locations of the geophones that Riverman et al. (2019) used to estimate the density profile across the NEGIS. Note that the colorbar's limits are different in the maps.

Bearing this in mind, we will try to assess this hypothesis's validity by applying the Gagliardini and Meyssonnier (1997) model to the strain rate configuration observed at the NEGIS. We will validate the results by comparing them to the density profile data provided by Riverman et al. (2019) and the surface elevation measurements from Hvidberg et al. (2020).

8.2 Density profile across the NEGIS

With the objective of analyzing the effect of the shear margins on the firn densification process, Riverman et al. (2019) performed a seismic survey across a section of the NEGIS, represented by white dots in the map shown in Figure 8.1. The resulting density profile is represented by the contour map of Figure 8.2, where we can identify a faster densification rate close to the shear margins. We will aim to reproduce this density profile by implementing the Gagliardini and Meyssonnier (1997) model in two dimensions, as explained in Chapter 5.

First of all, following the same arguments as in Chapter 6, we will consider a depth-constant temperature. Besides, both the temperature and the accumulation rate will be kept constant along the cross-section; specifically, $T = -28.8$ °C and $\dot{a} = 0.18$ w.eq., myr^{-1} (INTERACT, 2021). Consequently, the resulting density profile would be horizontally homogeneous unless we introduced varying strain rates.

Before diving into how the additional strain rates have been introduced, we will give some practical information about the calculation of the strain rates around the NEGIS. First of all, we have defined the spatial coordinates to be: x for the direction of the ice stream flow (positive into the paper), y for the *offset along line*, and z for the depth. Apart from this, we have calculated the longitudinal ($\dot{\epsilon}_{xx}$) and shear ($\dot{\epsilon}_{xy}$) strain rates based on the satellite-derived velocities from the MEAsuRES program (Howat, 2020). To do so, we have rotated the velocity field to match our choice of coordinates before calculating the spatial derivatives. Afterwards, we have smoothed the strain rates to avoid numerical instabilities (see top plot of Figure 8.2). Finally, we have considered depth-constant velocities, implying that $\dot{\epsilon}_{xz} = \dot{\epsilon}_{yz} = 0$.

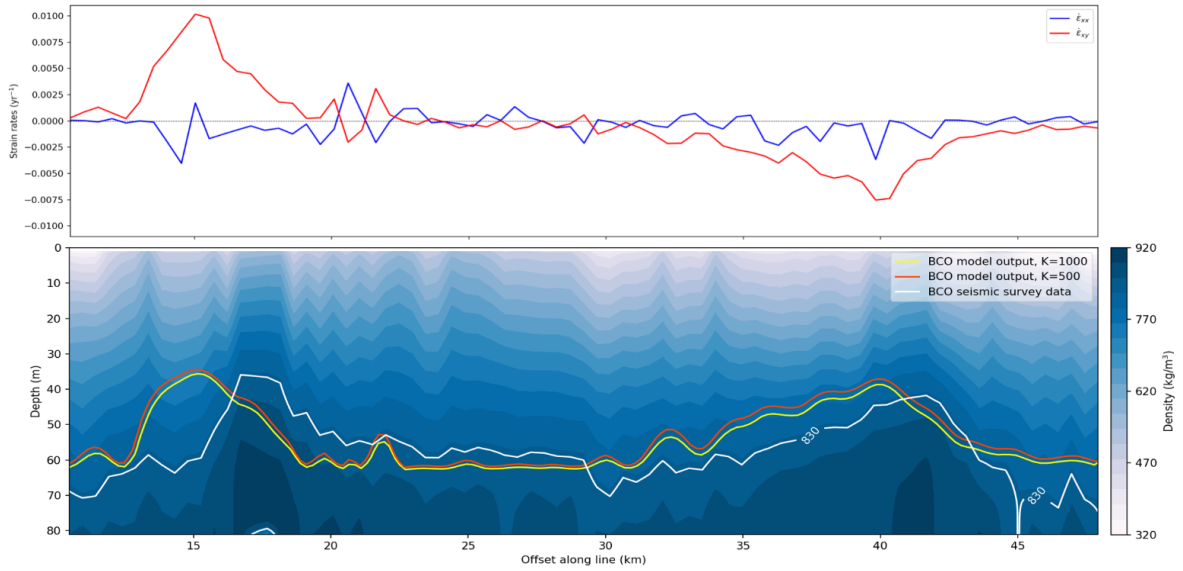

Figure 8.2: Top: Smoothed longitudinal ($\dot{\epsilon}_{xx}$) and shear ($\dot{\epsilon}_{xy}$) strain rates across the NEGIS, at the geophones' locations. Strain rates are obtained by rotating the surface velocity field so that the x direction corresponds to the direction of the ice flow (see Figure 8.1). **Bottom: BCO depth from seismic survey and model output.** The contour map shows the firn density profile at the NEGIS, derived from a seismic survey performed by Riverman et al. (2019). The white line is a contour line of density 830 kg m^{-3}, corresponding to the BCO depth. The yellow and orange lines represent the model output obtained after running the model for K=1000 and K=500, respectively.

As we will be working with a 2D model, the symmetric strain rate tensor, $\dot{\boldsymbol{\epsilon}}$, will be of dimension 2×2 and will only include the elements $\dot{\epsilon}_{yy}$, $\dot{\epsilon}_{zz}$, and $\dot{\epsilon}_{yz}$. However, the shear strain rates, $\dot{\epsilon}_{xy}$, are the predominant ones at the cross-section of the NEGIS, so we have to find a way to account for their effect without going 3D. To do so, we have artificially extended the model's dimensions by manually adding the terms that would arise if these operators were to be applied in a proper three-dimensional formulation. Therefore, taking into account that the affected variables are $\dot{\epsilon}_{\mathrm{m}} = \mathrm{tr}(\dot{\boldsymbol{\epsilon}})$ and $\dot{\boldsymbol{\epsilon}} : \dot{\boldsymbol{\epsilon}}$,

$$(\dot{\epsilon}_{\mathrm{m}})_{\mathrm{extended}} = \mathrm{tr}(\dot{\boldsymbol{\epsilon}}_{\mathrm{2D}}) + \dot{\epsilon}_{xx} \qquad \text{and} \qquad (\dot{\boldsymbol{\epsilon}} : \dot{\boldsymbol{\epsilon}})_{\mathrm{extended}} = \dot{\boldsymbol{\epsilon}}_{\mathrm{2D}} + \dot{\epsilon}_{xx}^2 + 2\ \dot{\epsilon}_{xy}^2$$

where $\dot{\boldsymbol{\epsilon}}_{\mathrm{2D}}$ stands for our model's standard two-dimensional strain rate tensor.

After running the simulation for K=500 and K=1000, we have plotted the resulting BCO depths on top of the reference density profile from Riverman et al. (2019), as shown in Figure 8.2. This plot shows that our model predicts higher densification rates at the shear margins, being the shallowest firn columns aligned with the shear strain rate maxima. However, even though the reference data shows an almost identical behavior, there seems to be a shift with respect to the aforementioned maxima. Finally, the BCO depth seems relatively insensitive to the magnitude of K, probably due to the depths at which it usually is located.

8.3 Surface elevation and age of firn at the BCO depth

Another way to assess the performance of our model is to analyze the strain-softening-induced surface elevation changes. The top plot of Figure 8.3 shows the steady state surface obtained from the model, which correctly predicts depressions in the shear margins. However, the estimated amplitudes of these perturbations is approximately half of those measured by Hvidberg et al. (2020).

Finally, having a shallower firn column implies that the ice will be younger at the BCO depth, which means that the previous results already verify the hypothesis of higher gas resolution in the areas with strong strain rates. However, it would be interesting to have an estimation of this age difference. Thus, we have calculated the age of the firn at the BCO depth by following particles that have departed from the surface along the steady-state velocity field. The results are shown in the bottom plot of Figure 8.3, where we can see that the age of the firn at the BCO depth may be up to 200 years younger at zones with high strain rates, which agrees well with the estimation made by Oraschewski and Grinsted (2022).

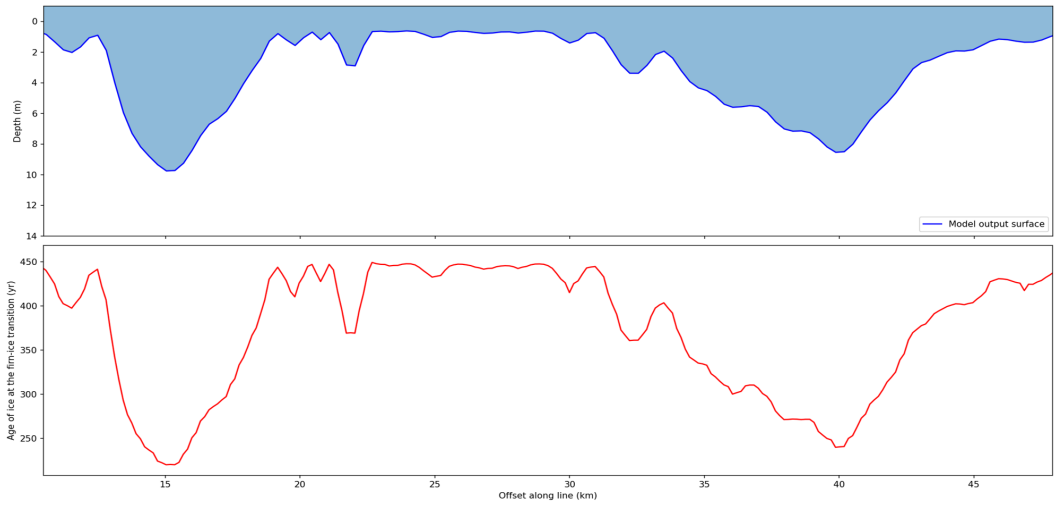

Figure 8.3: Top: Surface elevation changes across the NEGIS estimated by the model. The increased densification rates at the shear margins result in depressions of about 10 meters. **Bottom: Age of the ice at the firn-ice transition, i.e. at the BCO depth.** The age has been estimated by following particles from the surface along the steady state velocity field. The faster the densification rate, the younger the ice at the transition.

Part III

Discussion and Conclusions

9. Discussion

Having worked on a wide range of problems and subjects during this project, we will, for the sake of clarity, structure the discussion into three sections, each of them devoted to one of our subprojects.

9.1 Validation and recalibration of the model

Before diving into an assessment of the choice of the *compound parameter*, K, we will give a general overview of the performance of the Gagliardini and Meyssonnier (1997) model. It seems that the adequacy of the model can be divided into two distinct zones (see Figure 6.1).

For relative densities bigger than 0.8, the model clearly fails to reproduce the observed densification rates regardless of the value of K. The fact that 0.81 is the limit of the piece-wise definition of the coefficient functions (a and b) hints that this disagreement can be a consequence of the theoretically derived expressions adopted by Gagliardini and Meyssonnier (1997) (a_0 and b_0). Thus, even though they concluded that a_0 and b_0 were good enough to account for all the processes involved at the higher densities, our results seem to disagree with this claim (even for Site-2, the site they used to calibrate the model).

The reason behind this discrepancy is not clear to us. The calibration process in Gagliardini and Meyssonnier (1997) was based on *cold room* experiments, in which they calculated the values of the coefficient functions for different relative densities, $\hat{\rho}$. We do not know whether there might be some important difference between how these experiments were conducted and the actual *in-situ* conditions, but the calibration seemed to work for the density profile from Dôme du Goûter they used to validate the results (see Figure 5 from Gagliardini and Meyssonnier (1997)).

It must be mentioned, though, that in this project, we have used the more recent implementation proposed in Zwinger et al. (2007) and Gagliardini (2012), where, for reasons not explained in the literature, the limit of the piecewise coefficient functions was redefined to be $\hat{\rho}_c = 0.81$ (instead of the original 0.785). In an attempt to test if there was any reason to justify an earlier shift, we set $\hat{\rho}_c$ as an additional free parameter in the optimization process. The result of this analysis was that the optimal limit of all the sites seemed to cluster around a lower mean $\hat{\rho}_c = 0.79 \pm 0.02$. However, the sample size was too small, and the results looked overfitted. Therefore, we finally decided to stick to the newer and most prevalent formulation, but we think that a more extensive analysis would result in a slightly lower value of $\hat{\rho}_c$.

In the case of the relative densities lower than 0.8, instead, the model's performance does depend on the chosen K. This value defines the modeled densification rates at the upper part of the firn column, being faster the higher the K. However, this is not surprising if we realize that K defines the value of a and b at the surface. This means that having fixed expressions for $\hat{\rho} > 0.81$, the lower the densities, the more changes in K will impact the values of the coefficient functions (as shown in Figure B.1).

Anyhow, as already mentioned, data always fall between the profiles obtained for K=100 and K=1000, which suggests that the best value is somewhere in between. This already hints at a possible need for recalibration of the Gagliardini and Meyssonnier (1997) model, which motivates the deeper study we have made. During this project, we have considered a global K of magnitude 500. However, to assess the significance of our results, we first need to understand how confidently we can make such assumptions.

Regarding the universality of the *compound parameter*, the linear regression test has shown itself to be inconclusive. Since the uncertainties are high, no statistically significant differences prove the existence of a particular global value of K (see Figure 6.4). We can see a homogeneous improvement of the regression parameters towards the lower end of the spectrum, but this could be due to the small sample size. Nevertheless, the analysis of individual RMSE curves, independent of the sample size, supports the idea of a relatively similar best value of K for all sites. Although this is not proof of universality, and only six Greenlandic sites have been tested, we consider that justifies the assumption for the scope of this work.

Once we have decided to consider a universal K, its value has to be defined. Results from the NEEM's tunnel deformation simulations align with the trend of our previous results, suggesting that this value lies lower than the widely used K=1000 (see Figure 6.6). We do not know the depth at which the trial tunnel was dug, but we have considered it as deep as it reasonably can (eight meters, one more than the snowblowers' limit). Since this is the most stable hypothetical location of the tunnel, such an analysis gives an estimate of a higher bound of K. Consequently, we strongly believe that, at least for these Greenlandic sites, a global value of K would probably lie below 500. Specifically, we have chosen K=500 to be able to interpret our further results as limiting bounds.

Before finishing this part of the discussion, we would like to make two final remarks. First, our sample size is small, which can increase the uncertainties and limit our results' representativeness. In light of this, we tried to include more sites in the analysis by taking additional firn density profiles from the SUMup database (Montgomery et al., 2018). However, temperature profiles and accumulation rate measurements were not available for most sites, and output from the Danish Meteorological Institute's `HIRHAM5` model was not accurate enough for our purposes (Christensen et al., 2007). Therefore, we decided to stick to the sites where we had reliable *in situ* measurements.

Finally, we would like to emphasize that the inverted temperature for Site-2 perfectly matches the observed one for K=1000 (see Figure 6.2). This means that, had we done this analysis based only on this site, we would have probably obtained Gagliardini and Meyssonnier (1997)'s same result. However, we have already pointed out that there is no K for which the model is able to reproduce the whole density profile (not even for Site-2), which casts some doubt on whether this is as significant as it may seem at first.

9.2 Shape optimization

We will start this section by remarking that our aim in this project has not been to perform a thorough analysis to find an applicable optimal shape. Instead, we are just interested in developing a reliable method that could potentially be used for such a purpose.

As we have seen in Figures 7.5 and 7.6, our approach can find better-performing solutions, at least after the parameters have been fine-tuned. Specifically, this improvement seems to be related to the formation of an arch and a reduction in the tunnel's width (see Figure 7.4). The construction of more complex ceilings is a field yet to be explored, but the enhanced durability of narrower tunnels has already been characterized at EGRIP (Steffensen, 2022). Finally, consistent with the field observations too, the method also predicts a reduced sensitivity to the initial shape if *supporting walls* are introduced, direct consequence of the increased stability of the surrounding firn. The magnitude of the effect may have been magnified by the issues we will explain now, but our results suggest that this might be a simple first measure that can already improve the durability of any tunnel.

Regarding the evolution of the volume, it may be surprising, at first, to see that the circular shape is better at preserving the volume than our optimized proposal. However, one must remember that these two cases are not directly comparable because the latter is forced to keep the floor flat. If this constraint is dropped, our method does find an *egg-shaped* solution that outperforms the cylinder but is of little practical use due to the curved floor. This contrast between volume conservation and practicality is something we also observe in other shapes, and shows that the best way to evaluate the performance is to consider not only the volume but also other pragmatic preferences depending on the purpose of the tunnel.

Taking this into account, together with all the construction-related implicit constraints, this method would have to be applied to an extensive range of initial conditions to find the absolute best tunnel for each particular case. This includes many configurations of the trenches' widths and depths, with varying widths of supporting walls, among others. Unfortunately, our method still can not handle all these cases systematically because the appropriate values of the regularization parameters are very dependent on the conditions involved. This issue could be smoothed by improving our definition of the cost function J (e.g., normalizing the line integrals over the boundaries with respect to the perimeter). However, our experience has been that there will always remain some dependence to be managed, and no set of parameters will give a satisfactory result for the whole range of conditions.

It is also important to mention that some further computational issues arise from the meshes' temporal evolution. There are those related to certain *rigidities* of `FEniCS`. For example, the fact that we have not found a way to keep track of the order of the hole's boundary nodes has created much trouble during the remeshing process.

However, the problems related to overlapping nodes during the evolution have been the most difficult to handle. In our formulation, this has been impossible to fix, not even paying the computational price of reducing the timestep, increasing the mesh resolution, or remeshing at every iteration. The only workaround we could find was to remove the parts that would eventually overlap by rounding the corners. Nonetheless, this is not satisfactory either because it creates the volume sink that gives rise to the artifacts we have seen in Figure 7.6. Having said this, we are aware that Brondex et al. (2020) were able to run highly detailed meshes for much more extended periods, even with the hole crossing itself at the corners. Thus, if not with `FEniCS`, there must be some other way of successfully handling these issues.

In short, we can conclude that this method can offer some insights regarding possible structural improvements that can be implemented in future tunnels. However, the optimization still needs to be refined if it is to be applied to a more extensive study, and the time evolution should be improved to avoid any corner smoothing requirement.

9.3 Strain softening

The strain softening problem was the primary motivation to use the Gagliardini and Meyssonnier (1997) model since it enables the inclusion of horizontal stresses. In fact, this model has allowed us to easily reproduce the faster densification rates at the NEGIS' shear margins. However, it is essential to note that these results can not be recreated if a linear-viscous fluid ($n = 1$) is considered. The reason is that, in such a case, the viscosity does not depend on the effective strain rate anymore (see equation 3.6). Consequently, we lose the contribution of the prevailing shear strain rates, $\dot{\epsilon}_{xy}$, which are responsible for the strain softening in this case.

The main success of the model is that the estimated BCO depth values are in good agreement with the field measurements (see Figure 8.2). Nevertheless, the apparent shift between the model output and observed densities requires a more in-depth assessment. A possible reason behind this disagreement could be a coordinate error when calculating the strain rates. However, it must be mentioned that Riverman et al. (2019) and Oraschewski and Grinsted (2022) obtained this same shift between the strain rate maxima and the shallowest firn column observations. The former overcame this issue by considering how the strain rates have changed during the estimated lifetime of the firn column (400 years). Unfortunately, the latter did not succeed in replicating these results, which suggests that more research is needed. Nonetheless, we should not leave this shift to tarnish that our model can adequately estimate the magnitude of the BCO depth across the shear margins.

The estimation of the amplitude of the surface depressions is not as satisfactory, though. It is true that the model predicts a lowering, but its magnitude is only half of the observed by Hvidberg et al. (2020) (see Figure 8.3). At first, we thought that this could be related to the value of K again, but not even

$K = 1000$ was capable of reproducing such amplitudes. We also tried to increase the model's sensitivity by including temperature anomalies of up to 4°C at the shear margins, similar to those detected by Holschuh et al. (2019). The idea was that higher temperatures would lower the viscosity of the firn, which could result in high enough densification rates. However, this hardly affected the final results, so we discarded this hypothesis too. Thus, we do not have a proper explanation for these amplitudes, but it could be that this feature is enhanced by some other mechanism not included in our model.

We would like to finish the discussion by addressing the consequences of the strain-rate-induced shallower firn column. As already mentioned in the text, the faster the densification rate, the younger the firn at the BCO depth (see Figure 8.3). Thus, at zones with high horizontal stresses, the air trapped in the bubbles has been in contact with the atmosphere for much less time (i.e., the age difference between the gas and surrounding, Δage, ice is lower).

The smaller Δage implies that the resolution of gas measurements is higher there. However, this improvement may not be significant because it does not compensate for all the interpretation challenges intrinsic to these highly dynamic areas. The real transcendental implication of the flow-dependent Δage is that if the stress configuration of an area changes with time, so does the age difference. Thus, even if areas of high present-day activity are avoided, the firn densification models used to interpret ice core data should be able to include strain softening effects due to the possibility of a varying flow history. This would better estimate the time-varying Δage and ensure a more precise ice core data interpretation, as suggested by Oraschewski and Grinsted (2022).

10. Conclusions and outlook

In this project, we have tested how to apply the Gagliardini and Meyssonnier (1997) model to several present-day problems. Unlike most of the traditional one-dimensional firn densification models, this can be easily extended to higher dimensions and implicitly considers arbitrary stresses. Also, even though it was not required in our case because the thermal coupling was weak, this model allows an easy introduction of additional equations. Having said this, it is clearly a versatile model that enables the study of custom and complex scenarios.

As a first step, we have revisited the calibration originally proposed by Gagliardini and Meyssonnier (1997), which has been widely used in firn densification studies ever since. After increasing the number of sites used to perform this calibration, we have concluded that a global set of parameters corresponding to K=500 seems to perform better than the original proposal. However, our study is still limited to a small sample of Greenlandic ice cores and should be extended to check if both the value and the universality assumption still hold.

Concerning the tunnel's shape optimization, we have proposed a method that, by minimizing the initial collapse rate, is able to find a shape that improves the volume conservation. This shape consists of an arch structure with a narrower base and favors the addition of *supporting walls*, which is intuitive and in agreement with field observations. However, the method still needs to be further developed before systematically being applied to an extensive study of a broader range of conditions.

In the last analysis, we have successfully reproduced the density profiles across the NEGIS by introducing horizontal strain rates into the model. Moreover, we have shown that the strain-softening effect can partially explain the depressions observed in the surface topography, but more research is needed to fully understand the feature's magnitude. Finally, we have confirmed that the BCO depth, and therefore, the age of the firn at that point, depends on the local stress configuration. Being this age difference fundamental for correct ice core data interpretation, firn densification models used for this purpose should be able to account for horizontal stresses as an additional forcing, apart from the usual accumulation rate and surface temperatures.

11. References

Abram, N., Gattuso, J.-P., Prakash, A., Cheng, L., Chidichimo, M.P., Crate, S., Enomoto, H., Garschagen, M., Gruber, N., Harper, S., Holland, E., Kudela, R.M., Rice, J., Steffen, K., and Schuckmann, K.von . Framing and context of the report. In Pörtner, H.-O., Roberts, D.C., Masson-Delmotte, V., Zhai, P., Tignor, M., Poloczanska, E., Mintenbeck, K., Alegría, A., Nicolai, M., Okem, A., Petzold, J., Rama, B., and Weyer, N.M., editors, *IPCC Special Report on the Ocean and Cryosphere in a Changing Climate*. 2019.

Alley, R. Firn densification by grain-boundary sliding: a first model. *Journal de Physique Colloques*, 48: C1–249–C1–256, 1987. doi: 10.1051/jphyscol:1987135.

Alley, R. B. and Bentley, C. R. Ice-core analysis on the siple coast of west antarctica. *Annals of Glaciology*, 11:1–7, 1988. doi: 10.3189/S0260305500006236.

Alnaes, M. S., Blechta, J., Hake, J., Johansson, A., Kehlet, B., Logg, A., Richardson, C., Ring, J., Rognes, M. E., and Wells, G.N. The FEniCS project version 1.5. *Archive of Numerical Software*, 3, 2015. doi: 10.11588/ans.2015.100.20553.

Arnaud, L., Barnola, J.M., and Duval, P. Physical modeling of the densification of snow/firn and ice in the upper part of polar ice sheets. pages 285–305, 2000.

Barnola, J. M., Pimienta, P., Raynaud, D., and Korotkevich, Y. S. Co2-climate relationship as deduced from the vostok ice core: a re-examination based on new measurements and on a re-evaluation of the air dating. *Tellus B: Chemical and Physical Meteorology*, 43(2):83–90, 1991. doi: 10.3402/tellusb.v43i2.15249.

Blunier, T. and Schwander, J. Gas enclosure in ice: age difference and fractionation. pages 307–326, 2000.

Bradley, A.M. *PDE-constrained optimization and the adjoint method*. Stanford University, Computer Science, Lecture notes, 10 2019.

Bréant, C., Martinerie, P., Orsi, A., Arnaud, L., and Landais, A. Modelling firn thickness evolution during the last deglaciation: constraints on sensitivity to temperature and impurities. *Climate of the Past*, 13 (7):833–853, 2017. doi: 10.5194/cp-13-833-2017. URL `https://cp.copernicus.org/articles/13/833/2017/`.

Brondex, J., Gagliardini, O., Gillet-Chaulet, F., and Chekki, M. Comparing the long-term fate of a snow cave and a rigid container buried at dome c, antarctica. *Cold Regions Science and Technology*, 180: 103164, 2020.

Christensen, O., Drews, M., Christensen, J., Dethloff, K., Hebestadt, I., Ketelsen, K., and Rinke, A. The hirham regional climate model version 5 (beta). *DMI Technical Report 06-17*, 01 2007.

Clausen, H.B., Gundestrup, N.S., Johnsen, S.J., Bindschadler, R., and Zwally, J. Glaciological investigations in the crête area, central greenland: A search for a new deep-drilling site. *Annals of Glaciology*, 10:10–15, 1988. doi: 10.3189/S0260305500004080.

Cuffey, K. M. and Paterson, W. S. B. *The physics of glaciers*. Butterworth-Heinemann, Oxford, 4th edition, 2010.

Dahl-Jensen, D., Mosegaard, K., Gundestrup, N., Clow, G. D., Johnsen, S. J., Hansen, A. W., and Balling, N. Past temperatures directly from the greenland ice sheet. *Science*, 282(5387):268–271, 1998. doi: 10.1126/science.282.5387.268.

Dahl-Jensen, D., Gundestrup, N., Gogineni, S. P., and Miller, H. Basal melt at northgrip modeled from borehole, ice-core and radio-echo sounder observations. *Annals of Glaciology*, 37:207–212, 2003. doi: 10.3189/172756403781815492.

Dokken, J.S. Drag minimization over an obstacle in stokes-flow, 2017. URL `http://www.dolfin-adjoint.org/en/latest/documentation/stokes-shape-opt/stokes_problem.html`.

Dokken, J.S., Mitusch, S.K., and Funke, S.W. Automatic shape derivatives for transient pdes in fenics and firedrake. 2020.

Duva, J.M. and Crow, P.D. Analysis of consolidation of reinforced materials by power-law creep. *Mechanics of Materials*, 17(1):25–32, 1994. ISSN 0167-6636. doi: https://doi.org/10.1016/0167-6636(94)90011-6.

Farrell, P. E. Mathematical background: adjoints and their applications, 2017. URL `http://www.dolfin-adjoint.org/en/latest/documentation/maths/index.html#dolfin-adjoint-mathematical-background`.

Fish, J. and Belytschko, T. *A First Course in Finite Elements*. 08 2007. ISBN 9780470035801. doi: 10.1002/9780470510858.oth1.

Gagliardini, O. Porous law for snow and firn in elmer/ice, 04 2012.

Gagliardini, O. and Meyssonnier, J. Flow simulation of a firn-covered cold glacier. *Annals of Glaciology*, 24:242–248, 1997. doi: 10.3189/S0260305500012246.

Gerber, T. A., Hvidberg, C. S., Rasmussen, S. O., Franke, S., Sinnl, G., Grinsted, A., Jansen, D., and Dahl-Jensen, D. Upstream flow effects revealed in the eastgrip ice core using a monte carlo inversion of a two-dimensional ice-flow model. *The Cryosphere*, 15:3655–3679, 02 2021. doi: 10.5194/tc-15-3655-2021.

Geuzaine, C. and Remacle, J.-F. Gmsh: a three-dimensional finite element mesh generator with built-in pre- and post-processing facilities. *International Journal for Numerical Methods in Engineering*, 79 (11):1309–1331, 2009.

Gilbert, A., Gagliardini, O., Vincent, C., and Wagnon, P. A 3-d thermal regime model suitable for cold accumulation zones of polythermal mountain glaciers. *Journal of Geophysical Research*, 09 2014. doi: 10.1002/2014JF003199.

Gleick, P.H. Water resources. In Schneider, S.H., editor, *Encyclopedia of Climate and Weather*, volume 2, pages 817–823. Oxford University Press, New York, 1996.

Grinsted, A., Hvidberg, C.S., Lilien, D., Rathmann, N., Karlsson, N., Gerber, T., Kjær, H., Vallelonga, P., and Dahl-Jensen, D. Accelerating ice flow at the onset of the northeast greenland ice stream. *Nature Communications*, 13, 09 2022. doi: 10.1038/s41467-022-32999-2.

Heil, M. *Course on Viscous Fluid Flow*. University of Manchester, Lecture notes, 2019.

Herron, M.M. and Langway, C.C. Firn densification: An empirical model. *Journal of Glaciology*, 25(93): 373–385, 1980. doi: 10.3189/S0022143000015239.

Holschuh, N., Lilien, D., and Christianson, K. Thermal weakening, convergent flow, and vertical heat transport in the northeast greenland ice stream shear margins. *Geophysical Research Letters*, 46, 07 2019. doi: 10.1029/2019GL083436.

Howat, I. Measures greenland ice velocity: Selected glacier site velocity maps from optical images, version 3, 2020. URL `https://nsidc.org/data/NSIDC-0646/versions/3`.

Hvidberg, C. S., Grinsted, A., Dahl-Jensen, D., Khan, S. A., Kusk, A., Andersen, J. K., Neckel, N., Solgaard, A., Karlsson, N. B., Kjær, H. A., and Vallelonga, P. Surface velocity of the northeast greenland ice stream (negis): assessment of interior velocities derived from satellite data by gps. *The Cryosphere*, 14(10):3487–3502, 2020. doi: 10.5194/tc-14-3487-2020. URL `https://tc.copernicus.org/articles/14/3487/2020/`.

INTERACT,. Egrip field station, 2021. URL `https://eu-interact.org/field-sites/egrip-field-station/`.

Johnsen, S. J. GRIP Temperature Profile, 2003. URL `https://doi.org/10.1594/PANGAEA.89007`.

Langway, C.C. Stratigraphic analysis of a deep ice core from greenland. 1967.

Lautrup, B. *Physics of continuous matter, second edition: Exotic and everyday phenomena in the macroscopic world*. 03 2011.

Li, J. and Zwally, H.J. Modeling of firn compaction for estimating ice-sheet mass change from observed ice-sheet elevation change. *Annals of Glaciology*, 52(59):1–7, 2011. doi: 10.3189/172756411799096321.

Licciulli, C., Bohleber, P., Lier, J., Gagliardini, O., Hoelzle, M., and Eisen, O. A full stokes ice-flow model to assist the interpretation of millennial-scale ice cores at the high-alpine drilling site colle gnifetti, swiss/italian alps. *Journal of Glaciology*, 66(255):35–48, 2020.

Lipovsky, B. P. Density matters: ice compressibility and glacier mass estimation. *Journal of Glaciology*, 68(270):831–832, 2022. doi: 10.1017/jog.2021.132.

Lundin, J., Stevens, C., Arthern, R., Buizert, C., Orsi, A., Ligtenberg, S., Simonsen, S., Cummings, E., Essery, R., Leahy, W., Harris, P., Helsen, M.M., and Waddington, E. Firn model intercomparison experiment (firnmice). *Journal of Glaciology*, 63:1–22, 02 2017. doi: 10.1017/jog.2016.114.

Maeno, N. and Ebinuma, T. Pressure sintering of ice and its implication to the densification of snow at polar glaciers and ice sheets. *The Journal of Physical Chemistry*, 87(21):4103–4110, 1983. doi: 10.1021/j100244a023.

Marqués, R, Melchor, J, Sánchez-Montesinos, I, Roda, O, Rus, G, and Hernández-Cortés, P. Biomechanical finite element method model of the proximal carpal row and experimental validation. *Front. Physiol.*, 12:749372, 01 2022. doi: 10.3389/fphys.2021.749372.

Mitusch, S.K., Funke, S.W., and Dokken, J.S. dolfin-adjoint 2018.1: automated adjoints for fenicsand firedrake. *Journal of Open Source Software*, 4(38):1292, 2019. doi: 10.21105/joss.01292.

Montgomery, L., Koenig, L., and Alexander, P. The sumup dataset: compiled measurements of surface mass balance components over ice sheets and sea ice with analysis over greenland. *Earth System Science Data*, 10(4):1959–1985, 2018. doi: 10.5194/essd-10-1959-2018. URL `https://essd.copernicus.org/articles/10/1959/2018/`.

NASA,. Nasa sea level change portal, Jan 2021. URL `https://sealevel.nasa.gov/understanding-sea-level/global-sea-level/ice-melt`.

Naumenko, K. and Altenbach, H. *Modeling of Creep for Structural Analysis*. 01 2007. ISBN 9783540708391. doi: 10.1007/978-3-540-70839-1_1.

Oraschewski, F. M. and Grinsted, A. Modeling enhanced firn densification due to strain softening. *The Cryosphere*, 16(7):2683–2700, 2022. doi: 10.5194/tc-16-2683-2022. URL `https://tc.copernicus.org/articles/16/2683/2022/`.

Orsi, A.J., Kawamura, K., Masson-Delmotte, V., Fettweis, X., Box, J.E., Dahl-Jensen, D., Clow, G.D., Landais, A., and Severinghaus, J.P. The recent warming trend in north greenland. *Geophysical Research Letters*, 44(12):6235–6243, 2017. doi: https://doi.org/10.1002/2016GL072212.

Porter, C., Morin, P., Howat, I., Noh, M.J., Bates, B., Peterman, K., Keesey, S., Schlenk, M., Gardiner, J., Tomko, K., Willis, M., Kelleher, C., Cloutier, M., Husby, E., Foga, S., Nakamura, H., Platson, M., Wethington, M.Jr., Williamson, C., Bauer, G., Enos, J., Arnold, G., Kramer, W., Becker, P., Doshi, A., D'Souza, C., Cummens, P., Laurier, F., and Bojesen, M. ArcticDEM, Version 3, 2018. URL `https://doi.org/10.7910/DVN/OHHUKH`.

Pozrikidis, C. *Flow at Low Reynolds Numbers. In: Fluid Dynamics.* Springer, Boston, MA, 2001. ISBN 978-1-4757-3323-5. doi: 10.1007/978-1-4757-3323-5-9.

Rathmann, N. *Weighted residuals and the finite element method.* Niels Bohr Institute, University of Copenhagen, Lecture notes, 2021.

Riverman, K., Alley, R., Anandakrishnan, S., Christianson, K., Holschuh, N., Medley, B., Muto, A., and Peters, L. Enhanced firn densification in high-accumulation shear margins of the ne greenland ice stream. *Journal of Geophysical Research: Earth Surface*, 124, 02 2019. doi: 10.1029/2017JF004604.

Salamatin, A.N., Lipenkov, V.Y., and Duval, P. Bubbly-ice densification in ice sheets: I. theory. *Journal of Glaciology*, 43(145):387–396, 1997. doi: 10.3189/S0022143000034961.

Schwander, J., Sowers, T., Barnola, J.-M, Blunier, T., Fuchs, A., and Malaizé, B. Age scale of the air in the summit ice: Implication for glacial-interglacial temperature change. *Journal of Geophysical Research*, 1021:19483–19494, 08 1997. doi: 10.1029/97JD01309.

Schwander, Stauffer B.,J. Age difference between polar ice and the air trapped in its bubbles. *Nature*, 311:48–47, 1984. doi: 10.1038/311045a0.

Steffensen, J. P. Poster: Balloon cast subsurface ice drilling and ice core analysis trenches evolution and fate. In *International Partnerships in Ice Core Drilling Sciences (IPICS)*, October 2022.

Sørensen, L., Simonsen, S., Nielsen, K.a, Lucas-Picher, P., Spada, G., Adalgeirsdottir, G., Forsberg, R., and Hvidberg, C. Mass balance of the greenland ice sheet (2003–2008) from icesat data—the impact of interpolation, sampling and firn density. *The Cryosphere*, 5:173–186, 03 2011. doi: 10.5194/tc-5-173-2011.

Wilkinson, D. A pressure-sintering model for the densification of polar firn and glacier ice. *Journal of Glaciology*, 34, 01 1988. doi: 10.1017/S0022143000009047.

Winkelmann, R., Martin, M. A., Haseloff, M., Albrecht, T., Bueler, E., Khroulev, C., and Levermann, A. The potsdam parallel ice sheet model (pism-pik) part 1: Model description. *The Cryosphere*, 5:715–726, 2011. doi: 10.5194/tc-5-715-2011.

Zwinger, T., Greve, R., Gagliardini, O., Shiraiwa, T., and Lyly, M. A full stokes-flow thermo-mechanical model for firn and ice applied to the gorshkov crater glacier, kamchatka. *Annals of Glaciology*, 45: 29–37, 2007.

Part IV

Additional material

A. Derivation of governing equations

This appendix provides the derivation of the governing equations of the density, $\rho(\boldsymbol{x}, t)$, velocity, $\boldsymbol{u}(\boldsymbol{x}, t)$, and temperature, $T(\boldsymbol{x}, t)$, fields: the continuity equation, the Stokes equation and the heat equation, respectively. We will show that these are just the mathematical representations of the conservation principles of mass, momentum, and internal energy. After that, the surface evolution equation will also be derived based on free-surface boundary conditions. One can find the weak form of these equations in the last section of this appendix.

A.1 Continuity equation: mass balance

Firn is a compressible porous fluid, so its density, ρ, varies within the fluid parcel. These variations in the density field are governed by the continuity equation, which arises from the principle of conservation of mass: *mass can neither be created nor destroyed*. Hence, the change in mass of a fluid parcel is a consequence of the imbalance between the inlet and outlet mass flows.

Consider a three dimensional control volume with dimensions $dV = dxdydz$ that is located in the velocity field $\boldsymbol{u}(x, y, z, t)$ and density field $\rho(x, y, z, t)$. Bearing in mind that the mass flux across an area, A, is defined as $\Phi = \rho \boldsymbol{u}\mathrm{A}$, the mass flux imbalance in the x direction can be written as

$$\Delta\Phi^x = \Phi(x) - \Phi(x + dx) = \rho u dydz - \left(\rho u + \frac{\partial(\rho u)}{\partial x} dx\right) dydz = -\frac{\partial(\rho u)}{\partial x} dxdydz = -\frac{\partial(\rho u)}{\partial x} dV \tag{A.1}$$

where the expression for $\Phi(x+dx)$ is obtained by applying the Taylor expansion and neglecting the terms $\mathcal{O}(dx^2)$. The negative sign implies that when the gradient of the mass flux is negative, mass accumulates inside the control volume. Thus, a non-zero mass flux across the control volume changes the control volume's mass over time, $(\partial\rho/\partial t)\ dV$. Accordingly, the continuity equation is obtained by generalizing A.1 into three dimensions.

$$\frac{\partial \rho}{\partial t} + \boldsymbol{\nabla} \cdot (\rho \boldsymbol{u}) = 0 \tag{A.2}$$

A.2 Stokes equation: momentum balance

The velocity field of firn is defined by the Stokes equation, $\boldsymbol{\nabla} \cdot \boldsymbol{\sigma} + \rho \boldsymbol{g} = \boldsymbol{0}$, where $\boldsymbol{\sigma}(\dot{\boldsymbol{\epsilon}})$, $\dot{\boldsymbol{\epsilon}}$, ρ, and $\boldsymbol{g}$ are the stress tensor, the strain rate tensor, the density field and the gravitational acceleration, respectively. This equation is a particular case of the Cauchy momentum equation, a relation based on the conservation of momentum. This principle states that any change in the momentum of the system results in forces acting on it: $d\boldsymbol{p}/dt = \mathbf{F}$. In what follows, we will analyze the change in momentum of an infinitesimal fluid control volume dV and the forces acting on it.

Regarding the change in the system's momentum, the analyzed volume is not fixed at some point. Therefore, this movement must be considered when calculating the temporal change of the momentum of the fluid element.

$$\frac{D\boldsymbol{p}}{Dt} = \rho \frac{D\boldsymbol{u}}{Dt} dV = \rho \left(\frac{\partial \boldsymbol{u}}{\partial t} + (\boldsymbol{u} \cdot \boldsymbol{\nabla})\boldsymbol{u}\right) dV \tag{A.3}$$

The forces acting on the fluid lump can be divided into surface and body forces, $\mathbf{F} = \mathbf{F}_{\text{surf}} + \mathbf{F}_{\text{body}}$. The former act on the surface of the lump, while the latter act on the entire body. In this case, the lump will flow under the influence of the gravitational field implying that $\mathbf{F}_{\text{body}} = \rho \boldsymbol{g} dV$. Apart from this, the surface forces are the viscous forces caused by imbalances in shear $(\sigma_{xy}, \sigma_{xz}, \sigma_{yz})$ and normal stresses $(\sigma_{xx}, \sigma_{yy}, \sigma_{zz})$. Thus, their contribution to the momentum balance can be obtained by a simple analysis of the differences in stresses exerted in the x, y, and z directions, similar to the one performed with the mass flux in the previous section.

$$\mathrm{F}^i_{\text{surf}} = \left(\frac{\partial \sigma_{xi}}{\partial x} + \frac{\partial \sigma_{yi}}{\partial y} + \frac{\partial \sigma_{zi}}{\partial z} \right) dV \qquad \Longrightarrow \qquad \mathbf{F}_{\text{surf}} = (\boldsymbol{\nabla} \cdot \boldsymbol{\sigma}) dV \tag{A.4}$$

where i stands for any of the x, y, and z directions, and dV is the volume of the infinitesimal lump. Thus,

$$\mathbf{F} = \mathbf{F}_{\text{surf}} + \mathbf{F}_{\text{body}} = (\boldsymbol{\nabla} \cdot \boldsymbol{\sigma} + \rho \boldsymbol{g}) dV \tag{A.5}$$

From expressions A.3 and A.5, one can deduce that

$$\rho \frac{D\boldsymbol{u}}{Dt} = \boldsymbol{\nabla} \cdot \boldsymbol{\sigma} + \rho \boldsymbol{g} \tag{A.6}$$

which is the Cauchy momentum equation and describes the momentum transport of a fluid under the effect of the gravitational field. However, glacier ice has a very low Reynolds number due to its high viscosity, so the momentum change rate is negligible compared to the applied forces (Pozrikidis, 2001). Consequently, equation A.6 reduces to the Stokes equation, which is the governing equation of the velocity field in this project.

$$\boldsymbol{\nabla} \cdot \boldsymbol{\sigma} + \rho \boldsymbol{g} = 0 \tag{A.7}$$

A.3 Heat equation: internal energy balance

The total energy of any system is composed of the mechanical and internal energy. The internal energy encompasses all the energy associated with the atoms and molecules, including their kinetic energy (related to the temperature) and the potential energy within and between them. According to the First Law of Thermodynamics, the internal energy of a system can only be modified by the interaction between the system and the environment, i.e., by the work done on or by the system and the heat flow in or out of the system. Thus, the rate of change of internal energy can be posed as $\dot{U}_{\text{int}} = \dot{Q} + \dot{W}$, where $\dot{Q}$ is the rate of heat exchange and $\dot{W}$ is the rate of work.

The temporal evolution of the temperature field of the system is closely related to the rate of change of internal energy. The First Law of thermodynamics can be rewritten as a function of the specific internal energy (internal energy per unit mass), U, since $U_{\text{int}} = \int \rho U dV$. Apart from this, the amount of heat necessary to raise the temperature of a unit of mass by one unit is called the specific heat capacity of the material, $c = dU/DT$. Therefore, the temperature field is completely defined if the work and heat exchange rates are known.

$$\int_\Omega \rho c \frac{DT}{dT} dV = \dot{Q} + \dot{W} \tag{A.8}$$

Regarding the heat exchange rate, $\dot{Q}$, the heat stored in the system varies due to heat flowing through the boundary or internal heat production during chemical or nuclear processes, among others. Fourier's law of heat conduction states that the current heat density, $\boldsymbol{q}$, is proportional to the negative temperature gradient, $\boldsymbol{q} \propto -\boldsymbol{\nabla} T$. Hence, if the internal heat production is neglected,

$$\dot{Q} = -\oint_{\partial\Omega} \boldsymbol{q} \cdot d\boldsymbol{S} = -\int_\Omega (\boldsymbol{\nabla} \cdot \boldsymbol{q}) dV = \int_\Omega \boldsymbol{\nabla} \cdot (k \boldsymbol{\nabla} T) dV \tag{A.9}$$

where k is the thermal conductivity of the material.

With respect to the rate of work, it obviously depends on the surface and body forces exerted on the system. However, the work done by body forces does not contribute to the change in internal energy, so only viscous stresses will be considered in this derivation.

$$\dot{W} = \oint_{\partial\Omega} \boldsymbol{u} \cdot \boldsymbol{\sigma} \cdot d\boldsymbol{S} = \int_{\Omega} (\boldsymbol{\nabla} \cdot (\boldsymbol{u} \cdot \boldsymbol{\sigma}) dV = \int_{\Omega} [\boldsymbol{\sigma} : \boldsymbol{\nabla}\boldsymbol{u} + \boldsymbol{u} \cdot (\boldsymbol{\nabla} \cdot \boldsymbol{\sigma}^{\top})] dV \tag{A.10}$$

The analysis of the conservation of the total energy (mechanical and internal) reveals that the term $\boldsymbol{u} \cdot (\boldsymbol{\nabla} \cdot \boldsymbol{\sigma}^{\top})$ is only related to a change in mechanical energy (Lautrup, 2011). On the contrary, the term $\boldsymbol{\sigma} : \boldsymbol{\nabla}\boldsymbol{u}$ represents the rate of loss of mechanical energy to heat as a consequence of viscous dissipation, i.e., corresponds to the change of the internal energy of the system. Thus, $\dot{W}_{\text{int}} = \int_{\Omega} \boldsymbol{\sigma} : \boldsymbol{\nabla}\boldsymbol{u} dV$. The heat equation is obtained by putting this last expression together with equations A.8 and A.9 and taking advantage of the fact that the strain rate tensor is the symmetric part of the gradient of the velocity.

$$\rho c \left(\frac{\partial T}{\partial t} + \boldsymbol{u} \cdot \boldsymbol{\nabla} T \right) = \boldsymbol{\nabla} \cdot (k_T \boldsymbol{\nabla} T) + \boldsymbol{\sigma} : \dot{\boldsymbol{\epsilon}} \tag{A.11}$$

The specific heat capacity of firn can be considered to be that of pure ice because the specific heat of the air in the pores is negligible. Thus, the specific heat capacity is given by $c = c_0 + c_1(T - T_0)$, where $c_0 = 2127.5\,\mathrm{J\,kg^{-1}\,K^{-1}}$, $c_1 = 7.253\,\mathrm{J\,kg^{-1}\,K^{-2}}$, and $T_0 = 273.16\,\mathrm{K}$ (Zwinger et al., 2007). Regarding the thermal conductivity, it depends not only on temperature but also on the density as follows,

$$k_{\mathrm{T}} = \frac{1 - k_{\mathrm{T},1}\rho + k_{\mathrm{T},2}\rho^2}{1 - k_{\mathrm{T},1}\rho_{\mathrm{ice}} + k_{\mathrm{T},2}\rho_{\mathrm{ice}}^2} k_{\mathrm{T},0} \exp(-\gamma_{\mathrm{T}} T) \tag{A.12}$$

where $k_{\mathrm{T},0} = 9.828\,\mathrm{W\,m^{-1}\,K^{-1}}$, $k_{\mathrm{T},1} = 7.3188 \times 10^{-3}\,\mathrm{m^3\,kg^{-1}}$, $k_{\mathrm{T},2} = 5.7 \times 10^{-5}\,\mathrm{m^6\,kg^{-2}}$, and $\gamma_{\mathrm{T}} = 5.7 \times 10^{-3}\,\mathrm{K^{-1}}$ (Zwinger et al., 2007).

A.4 Free surface equation

As ice flows, the surface of ice sheets and glaciers evolve, changing their shape until the steady state is reached. This evolution is governed by the surface evolution equation, derived by imposing the kinematic free surface boundary condition. Free surfaces are the surfaces present in the interface between two fluids, in this case, the surface between firn and atmosphere. The kinematic free surface boundary condition simply states that a fluid lump on the free surface can not jump, i.e., it must remain on the free surface (Heil, 2019).

Consider the two dimensional free surface, $F(x, z, t)$, defined as $F(x, z, t) = h(x, t) - z = 0$, where $z = h(x, t)$ is the height of the free surface for each position and time. If firn can not leave the free surface, then the convective derivative of the surface, F, must vanish.

$$\frac{DF}{Dt} = \frac{\partial F}{\partial t} + \boldsymbol{u}_{\mathrm{s}} \cdot \nabla F = 0 \Longleftrightarrow \frac{\partial h(x,t)}{\partial t} = w_{\mathrm{s}}(x) - u_{\mathrm{s}}(x) \frac{\partial h(x,t)}{\partial x} \tag{A.13}$$

where $\boldsymbol{u}_s$ refers to the surface velocity.

In the case of glaciers and ice sheets, snowfall and ablation also impact the development of the surface and, therefore, must be taken into account. To do so, an additional term, $\dot{b}$, is added to the left-hand side of the equation. This term will have negative values where ice melts and positive ones when snow accumulates due to precipitation.

$$\frac{\partial h(x,t)}{\partial t} = w_{\mathrm{s}}(x) - u_{\mathrm{s}}(x) \frac{\partial h(x,t)}{\partial x} + \dot{b} \tag{A.14}$$

This equation governs the evolution of the surface and implies that the flow velocities determine the shape of the surface of the fluid of interest. However, the flow velocities are then constrained by the surface's shape, so the surface evolution can be understood as a feedback loop between the velocities and the free surface.

A.5 Weak form of the equations

The weak forms of the governing equations are presented in this section. As mentioned in Chapter 4, the weak or variational form of the equations is obtained by multiplying the equation with some weight functions, w, and integrating over the entire space. Besides, the terms with second-order derivatives are integrated by parts to reduce them to first-order derivatives to avoid numerical issues due to the possible limited differentiability of the function of interest. As a last remark, the temporal derivatives have been discretized based on Euler's method. The subindices n and $n+1$ will represent the values of the previous and the following time steps, respectively.

Continuity equation

$$\int_\Omega \left(\frac{1}{\Delta t}\rho_{n+1} + \rho_{n+1}\boldsymbol{\nabla}\cdot\boldsymbol{u} + \boldsymbol{u}\cdot\boldsymbol{\nabla}\rho_{n+1} \right) w \; d\mathrm{A} = \int_\Omega \frac{1}{\Delta t}\rho_n \; w \; d\mathrm{A} \tag{A.15}$$

Stokes equation

$$\int_\Omega \boldsymbol{\sigma} : \boldsymbol{\nabla}\boldsymbol{w} \; d\mathrm{A} = \rho \int_\Omega \boldsymbol{g} \; \boldsymbol{w} \; d\mathrm{A} \tag{A.16}$$

Heat equation

$$\int_\Omega \left[\left(\frac{1}{\Delta t}T_{n+1} + \boldsymbol{u}\cdot\boldsymbol{\nabla}T_{n+1} - \frac{1}{\rho c}(\boldsymbol{\sigma} : \dot{\boldsymbol{\epsilon}} + \boldsymbol{\nabla}T_{n+1}\cdot\boldsymbol{\nabla}k) \right) w + \frac{k}{\rho c}\boldsymbol{\nabla}T_{n+1}\cdot\boldsymbol{\nabla}w \right] d\mathrm{A} = \int_\Omega \frac{1}{\Delta t}T_n \; w \; d\mathrm{A} \tag{A.17}$$

Surface evolution equation

$$\int_\Omega \left(h_{n+1} + \Delta t u_x \frac{\partial h_{n+1}}{\partial x} + \Delta t \dot{b} \right) w \; d\mathrm{A} = \int_\Omega (h_n + \Delta t u_z) \; w \; d\mathrm{A} \tag{A.18}$$

B. Insight into firn rheology

This chapter provides information for a deeper understanding of the firn rheology adopted in this project. First of all, a detailed derivation of the rheology is provided, where $\boldsymbol{\sigma}(\dot{\boldsymbol{\epsilon}})$ is obtained starting from the Norton-Bailey creep potential, and the effective stress for general porous material proposed by Duva and Crow (1994). Later, it is explained how the coefficient functions a and b have been implemented in order to avoid instabilities.

B.1 Derivation of the rheology

The first assumption in the derivation of the rheology of firn is that the effective stress, σ_{E}, and the effective strain rate, $\dot{\epsilon}_{\mathrm{E}}$, are related through a Norton-Bailey creep potential. Following Naumenko and Altenbach (2007), an expression for the strain rate tensor, $\dot{\boldsymbol{\epsilon}}$, can be obtained by rewriting this power law.

$$\dot{\epsilon}_{\mathrm{E}} = C\sigma_{\mathrm{E}}^{n} \qquad \Longrightarrow \qquad \dot{\boldsymbol{\epsilon}} = \frac{C}{2}\sigma_{\mathrm{E}}^{n-1}\frac{\partial \sigma_{\mathrm{E}}^{2}}{\partial \boldsymbol{\sigma}} \tag{B.1}$$

where C is the flow-rate factor that will be redefined at the end of the derivation so that Glen's flow law is recovered when the density of ice is reached. n is the creep exponent and, based on field data, it is usually assumed to be $n = 3$ in glaciology (Cuffey and Paterson, 2010).

The forward rheology, $\dot{\boldsymbol{\epsilon}}(\boldsymbol{\sigma})$ can, therefore, be obtained if the expression of the effective stress is known. Assuming that the effective stress is a function of the first, $\mathrm{tr}(\dot{\boldsymbol{\epsilon}})$, and the second, $\dot{\boldsymbol{\epsilon}} : \dot{\boldsymbol{\epsilon}}$, invariants, Duva and Crow (1994) proposed the following relation for general porous materials:

$$\sigma_{\mathrm{E}}^{2} = \frac{3a}{2}\left(\boldsymbol{\sigma} : \boldsymbol{\sigma} - \frac{\mathrm{tr}(\boldsymbol{\sigma})^{2}}{3}\right) + b\left(\frac{\mathrm{tr}(\boldsymbol{\sigma})}{3}\right)^{2} \tag{B.2}$$

Note that in Glen's law the effective stress only depends on the second isotropic tensor invariant due to incompressibility.

Taking into account that $\partial(\boldsymbol{\sigma} : \boldsymbol{\sigma})/\partial\boldsymbol{\sigma} = 2\boldsymbol{\sigma}$ and $\partial \mathrm{tr}(\boldsymbol{\sigma})^{2}/\partial\boldsymbol{\sigma} = 2\mathrm{tr}(\boldsymbol{\sigma})\mathbb{1}$, the forward rheology is written as follows (notice that a factor $3/2$ has been absorbed into C):

$$\dot{\boldsymbol{\epsilon}}(\boldsymbol{\sigma}) = C\sigma_{\mathrm{E}}^{n-1}\left[a\left(\boldsymbol{\sigma} - \frac{\mathrm{tr}(\boldsymbol{\sigma})}{3}\mathbb{1}\right) + \frac{2b}{3^{2}}\frac{\mathrm{tr}(\boldsymbol{\sigma})}{3}\mathbb{1}\right] \tag{B.3}$$

However, the variable of interest in this project is the inverse rheology, $\boldsymbol{\sigma}(\dot{\boldsymbol{\epsilon}})$, because it is the one to be introduced in the momentum balance equation, 3.2. The first step to get the inverse rheology is to vectorize equation B.3 based on $\boldsymbol{\mathcal{V}}(\boldsymbol{X}) = (X_{11}, X_{21}, X_{31}, X_{12}, X_{22}, X_{32}, X_{13}, X_{23}, X_{33})^{\top}$.

$$\boldsymbol{\mathcal{V}}(\dot{\boldsymbol{\epsilon}}) = C\sigma_{\mathrm{E}}^{n-1}\mathbf{P}\boldsymbol{\mathcal{V}}(\boldsymbol{\sigma}) \qquad \text{where} \qquad \mathbf{P} = a\mathbb{1}_{9} + \left(\frac{2b}{3^{3}} - \frac{a}{3}\right)\boldsymbol{\mathcal{V}}(\mathbb{1}) \otimes \boldsymbol{\mathcal{V}}(\mathbb{1}) \tag{B.4}$$

where $\otimes$ is the outer product.

Hence, the inverse rheology is obtained by rearranging this expression as $\boldsymbol{\sigma} = C^{-1}\sigma_{\mathrm{E}}^{1-n}\boldsymbol{\mathcal{V}}^{-1}(\mathbf{P}^{-1}\boldsymbol{\mathcal{V}}(\dot{\boldsymbol{\epsilon}}))$, and taking into account that $\dot{\epsilon}_{\mathrm{E}} = C\sigma_{\mathrm{E}}^{n}$.

$$\boldsymbol{\sigma}(\dot{\boldsymbol{\epsilon}}) = C^{-1/n}\dot{\epsilon}_{\mathrm{E}}^{(1-n)/n}\left[\frac{1}{a}\left(\dot{\boldsymbol{\epsilon}} - \frac{\mathrm{tr}(\dot{\boldsymbol{\epsilon}})}{3}\mathbb{1}\right) + \frac{3}{2b}\mathrm{tr}(\dot{\boldsymbol{\epsilon}})\mathbb{1}\right] \tag{B.5}$$

$$\dot{\epsilon}_{\mathrm{E}}^2 = \frac{2}{3a}\left(\dot{\boldsymbol{\epsilon}} : \dot{\boldsymbol{\epsilon}} - \frac{\mathrm{tr}(\dot{\boldsymbol{\epsilon}})^2}{3}\right) + \frac{1}{b}\mathrm{tr}(\dot{\boldsymbol{\epsilon}})^2 \tag{B.6}$$

This expression of the inverse constitutive equation matches the one proposed by Duva and Crow (1994).

Finally, the flow-rate factor, C, has to be defined in a way that Glen's flow law,

$$\boldsymbol{\sigma} = A^{-1/n}\epsilon_{\mathrm{E}_{\mathrm{ice}}}^{(1-n)/n}\dot{\boldsymbol{\epsilon}} \qquad \text{where} \qquad \dot{\epsilon}_{\mathrm{E}_{\mathrm{ice}}}^2 = \frac{1}{2}\dot{\boldsymbol{\epsilon}} : \dot{\boldsymbol{\epsilon}} \tag{B.7}$$

is recovered when the density of ice is reached. By definition, in the limit $\rho \to \rho_{\mathrm{ice}}$, $a \to 1$ and $b \to 0$. Also, since the fluid becomes incompressible, the divergence of velocity vanishes, $\mathrm{tr}(\dot{\boldsymbol{\epsilon}}) \to 0$. Thus, in this limit, the inverse rheology is written as follows:

$$\lim_{\rho\to\rho_i}\boldsymbol{\sigma} = C^{-1/n}\dot{\epsilon}_{\mathrm{E}}^{(1-n)/n}\dot{\boldsymbol{\epsilon}} \qquad \text{where} \qquad \lim_{\rho\to\rho_i}\dot{\epsilon}_{\mathrm{E}}^2 = \frac{2}{3}\dot{\boldsymbol{\epsilon}} : \dot{\boldsymbol{\epsilon}}. \tag{B.8}$$

In order these two expressions to be equivalent, the flow parameter must be modified as $C^{-1/n} \to A^{-1/n}\frac{1}{2}^{(1-n)/2n}\frac{3}{2}^{(1-n)/2n} = A^{-1/n}\frac{3}{4}^{(1-n)/2n}$. Therefore, the final expression for the inverse rheology of firn is:

$$\boldsymbol{\sigma}(\dot{\boldsymbol{\epsilon}}) = \frac{3}{4}^{(1-n)/2n}A^{-1/n}\dot{\epsilon}_{\mathrm{E}}^{(1-n)/n}\left[\frac{1}{a}\left(\dot{\boldsymbol{\epsilon}} - \frac{\mathrm{tr}(\dot{\boldsymbol{\epsilon}})}{3}\mathbb{1}\right) + \frac{3}{2b}\mathrm{tr}(\dot{\boldsymbol{\epsilon}})\mathbb{1}\right] \tag{B.9}$$

$$\dot{\epsilon}_{\mathrm{E}}^2 = \frac{2}{3a}\left(\dot{\boldsymbol{\epsilon}} : \dot{\boldsymbol{\epsilon}} - \frac{\mathrm{tr}(\dot{\boldsymbol{\epsilon}})^2}{3}\right) + \frac{1}{b}\mathrm{tr}(\dot{\boldsymbol{\epsilon}})^2 \tag{B.10}$$

Although the flow parameter A is greatly influenced by temperature and crystal fabric, in this project, only the effect of temperature is considered for simplicity and because it is easily quantified (Cuffey and Paterson, 2010).

B.2 Computation of the coefficient functions a and b

One of the aims of this Master's Thesis project is to recalibrate the fitted constants of the coefficient functions a and b (see equations below). In order to do so, the number of free parameters has been reduced from four to one by imposing different conditions, such as the continuity of a and b at the critical density, $\hat{\rho}_{\mathrm{c}} = 0.81$. Apart from this, the kink these functions have around this critical density is sometimes a source of numerical instabilities, so a smooth transition between the two zones has been imposed.

$$a(\hat{\rho}) = \begin{cases} a_1 = e^{C_1 - C_2\hat{\rho}} & \text{for} \quad 0.4 < \hat{\rho} \leq 0.81 \\ a_0 = \frac{1+2(1-\hat{\rho})/3}{\hat{\rho}^{2n/(n+1)}} & \text{for} \quad 0.81 < \hat{\rho} \leq 1 \end{cases} \qquad b(\hat{\rho}) = \begin{cases} b_1 = e^{C_3 - C_4\hat{\rho}} & \text{if} \quad 0.4 < \hat{\rho} \leq 0.81 \\ b_0 = \frac{3(1-\hat{\rho})^{1/n}}{4n[1-(1-\hat{\rho})^{1/n}]}^{\frac{2n}{n+1}} & \text{if} \quad 0.81 < \hat{\rho} \leq 1 \end{cases}$$

Smoothing of the piece-wise functions

Despite being possible to define piece-wise functions through conditionals in `FEniCS`, unwanted numerical instabilities arise from the ragged transition around the critical density, $\hat{\rho}_c = 0.81$. In order to avoid such issues, a step function is introduced to smooth this transition between a_0 and a_1 and b_0 and b_1. To do so, the scaling laws are rewritten as follows:

$$a_1 = k_a \exp[-\gamma_a(\hat{\rho} - \hat{\rho}_s)] \qquad \text{and} \qquad b_1 = k_b \exp[-\gamma_b(\hat{\rho} - \hat{\rho}_s)] \tag{B.11}$$

where $\hat{\rho}_s = 0.4$ is the relative density of the snow at the surface.

Then, due to the dominant and subdominant scaling behavior of a_0 and a_1, and b_0 and b_1, the coefficient functions can be written as

$$a = a_0 + \mu a_1 \qquad \text{and} \qquad b = b_0 + \mu b_1 \qquad \text{where} \qquad \mu = \frac{1}{1 + \exp[-\gamma_\mu(\hat{\rho}_c - \hat{\rho})]} \tag{B.12}$$

where μ is the logistic function that smoothens the transition, and γ_μ is the parameter that controls the level of smoothness, here taken to be $\gamma_\mu = 20$.

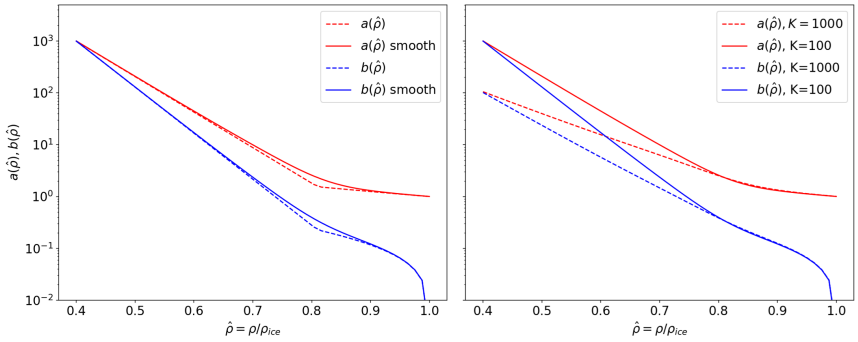

Figure B.1: Left: Original and smoothed coefficient functions. If a_0 and a_1 (b_0 and b_1) are combined through a logistic function, the transition is smooth, the properties of the coefficient functions are not altered, and numerical instabilities are avoided. **Right: a and b for different values of K.** K corresponds to the value of a and b at the density of snow and determines the slope of the empirical part of the coefficient functions.

Reduction of the number of free parameters

As explained in Chapter 5, in this project, the free parameters in the coefficient functions a and b are going to be recalibrated by fitting the model output to *in situ* depth-density measurements. More precisely, *in situ* temperature measurements will be compared to the temperatures predicted by the model for different values of k_a, k_b, γ_a, and γ_b. If the values of the parameters are changed randomly, the functions a and b will probably not meet the desired conditions. Therefore, before performing the fit, the number of free parameters has been reduced from four to one by imposing several conditions.

- a and b must be continuous functions, so $a_0(\hat{\rho}_c) = a_1(\hat{\rho}_c)$ and $a_0(\hat{\rho}_c) = a_1(\hat{\rho}_c)$, which means that

$$\gamma_a = \frac{\ln k_a - \ln a_0(\hat{\rho}_c)}{\hat{\rho}_c - \hat{\rho}_s} \qquad \text{and} \qquad \gamma_b = \frac{\ln k_b - \ln b_0(\hat{\rho}_c)}{\hat{\rho}_c - \hat{\rho}_s} \tag{B.13}$$

- The rate of viscous energy dissipation must be positive.

$$\boldsymbol{\sigma} : \dot{\boldsymbol{\epsilon}} = A^{-1/n}\left[a\ \dot{\boldsymbol{\epsilon}} : \dot{\boldsymbol{\epsilon}} + \left(\frac{3^2}{2b} - \frac{3}{a}\right)\left(\frac{\mathrm{tr}(\dot{\boldsymbol{\epsilon}})}{3}\right)^2\right]^{(n+1)/2} \geq 0 \iff \frac{a}{b} \geq \frac{2}{9} \tag{B.14}$$

  $a = b = 1$, which implies that $K = k_a = k_b$, fulfils the condition and is in good agreement with the works of Gagliardini and Meyssonnier (1997) and Zwinger et al. (2007). The parameter K defines defines the values of a and b at the densities of snow $K = a(\hat{\rho}_c) = b(\hat{\rho}_c)$ (see Figure B.1).

C. Adjoint-based optimization

In this thesis, two PDE constraint optimization problems have been solved: the fit of the flow-rate parameter A and the shape optimization of a tunnel. Since both problems have been solved based on the adjoint-based optimization method, a brief review of its mathematical background is provided in this appendix. After defining the problem, the finite difference and adjoint approaches will be introduced and compared. This appendix has been written based on the works of Farrell (2017) and Bradley (2019).

C.1 Definition of the problem

Assume that $F(\boldsymbol{u}(\boldsymbol{m}), \boldsymbol{m}) = 0$ is the system of governing equations, where $\boldsymbol{m} \in \mathbb{R}^M$ is a set of parameters (e.g. values of initial conditions, boundary conditions, and material properties) and $\boldsymbol{u}(\boldsymbol{m}) \in \mathbb{R}^{\mathrm{U}}$ is the solution of the forward problem (e.g. velocity, pressure, and density fields). The functional $J(\boldsymbol{u}(\boldsymbol{m}), \boldsymbol{m})$ represent the quantity to be optimized, for example, the misfit between measured and modeled data. The problem statement would then be, which is the set of parameters $\boldsymbol{m}$ that minimizes the functional $J(\boldsymbol{u}(\boldsymbol{m}), \boldsymbol{m})$ subject to the constraint that $F(\boldsymbol{u}(\boldsymbol{m}), \boldsymbol{m}) = 0$?

C.2 Minimization of the functional $J(\boldsymbol{u}(\boldsymbol{m}), \boldsymbol{m})$

$J(\boldsymbol{u}(\boldsymbol{m}), \boldsymbol{m})$ takes different values depending on $\boldsymbol{u}$ and $\boldsymbol{m}$, so it can be thought as a hyperdimensional landscape with peaks and valleys. The aim of this problem is to find the $\boldsymbol{m}$ that minimizes the functional, i.e., that corresponds to the deepest valley. One of the simplest methods to achieve so is the gradient descent method, which consists in taking steps from an initial guess until it reaches the best values by exploiting the information of the derivatives of J. There are several methods to compute $dJ/d\boldsymbol{m}$, finite differencing, and the adjoint approach, among others.

Finite difference approach

When applying finite differencing, the gradient is estimated by analyzing how small perturbations of each of the parameters, m_i, affect the functional, as shown in equation C.1. Even though it may be an intuitive and straightforward method, it becomes inefficient when the number of parameters, M, is high; the forward problem must be solved M times at every step.

$$\frac{J(\boldsymbol{u}(\boldsymbol{m}), \boldsymbol{m})}{dm_i} = \frac{J(\boldsymbol{u}(\boldsymbol{m} + he_i), \boldsymbol{m} + he_i) - J(\boldsymbol{u}(\boldsymbol{m}), \boldsymbol{m})}{h} \tag{C.1}$$

where h is the change applied to the parameters (the finite difference), and e_i is a vector whose only non-zero value is the i^{th} element.

The adjoint approach

The adjoint approach is an alternative way of estimating the gradient $dJ/d\boldsymbol{m}$. Despite not being as intuitive as the finite difference method, it dramatically reduces the number of times the forward problem must be solved. There are two ways of deriving this method: by developing the derivatives or based on a Lagrangian optimization approach. Being a more intuitive explanation, we have chosen to follow the latter.

The minimization of $J(\boldsymbol{u}(\boldsymbol{m}), \boldsymbol{m})$ under the constraint $F(\boldsymbol{u}(\boldsymbol{m}), \boldsymbol{m}) = 0$ can be posed as a Lagrangian minimization problem, $\mathcal{L}(\boldsymbol{u}, \boldsymbol{m}) = J(\boldsymbol{u}, \boldsymbol{m}) + \lambda^\top F(\boldsymbol{u}, \boldsymbol{m})$. Besides, the constraint $F(\boldsymbol{u}, \boldsymbol{m}) = 0$ implies that $d\mathcal{L}/d\boldsymbol{m} = dJ/d\boldsymbol{m}$. Therefore, an expression for the gradient of interest can be obtained by developing the derivative of the Lagrangian with respect to the vector of parameters.

$$\frac{dJ}{d\boldsymbol{m}} = \frac{d\mathcal{L}}{d\boldsymbol{m}} = \frac{\partial J}{\partial \boldsymbol{m}} + \lambda^\top \frac{\partial F}{\partial \boldsymbol{m}} + \left(\frac{\partial J}{\partial \boldsymbol{u}} + \lambda^\top \frac{\partial F}{\partial \boldsymbol{u}} \right) \frac{d\boldsymbol{u}}{d\boldsymbol{m}} \tag{C.2}$$

As J and F are normally simple expressions in terms of $\boldsymbol{u}$ and $\boldsymbol{m}$, all the derivatives in equation C.2 are usually easy to compute, except for $d\boldsymbol{u}/d\boldsymbol{m}$. The calculation of this last term can be avoided by imposing that the term $\partial J/\partial \boldsymbol{u} + \lambda^\top \partial F/\partial \boldsymbol{u}$ vanishes. Note that this condition arises naturally when deriving the adjoint method based on implicit derivatives. The adjoint of this condition is known as the adjoint equation (right-hand side of equation C.3).

$$\left(\frac{\partial J}{\partial \boldsymbol{u}} + \lambda^\top \frac{\partial F}{\partial \boldsymbol{u}} = 0 \right)^* \qquad \Longrightarrow \qquad \frac{\partial F}{\partial \boldsymbol{u}}^* \lambda + \frac{\partial J}{\partial \boldsymbol{u}}^* = 0 \tag{C.3}$$

Hence, the adjoint-based optimization method (see equation C.4) consists of three steps. First of all solve the forward problem, $F(\boldsymbol{u}, \boldsymbol{m}) = 0$, to get $\boldsymbol{u}$. Then, solve the adjoint equation and obtain λ. Finally, introduce this λ and evaluate $dJ/d\boldsymbol{m}$. This means that, no matter the number of parameters M, only two PDEs are solved in each iteration, in contrast to the M PDEs required by the finite difference approach.

$$\frac{dJ}{d\boldsymbol{m}} = \frac{\partial J}{\partial \boldsymbol{m}} + \lambda^\top \frac{\partial F}{\partial \boldsymbol{m}} \qquad \text{where} \qquad \frac{\partial F}{\partial \boldsymbol{u}}^* \lambda + \frac{\partial J}{\partial \boldsymbol{u}}^* = 0 \tag{C.4}$$

This last equation is the core of the adjoint method and entails that the change to be applied to the input parameters, $\boldsymbol{m}$, can be deduced by analyzing how the quantity of interest, J, changes by varying the solution, $\boldsymbol{u}$. This is quite the opposite of the finite difference approach where, in order to choose the variation of the input parameters, these are *blindly* changed to see how each of the perturbations finally affects the quantity of interest.

D. Code availability

A sample of the most representative codes used during this project will be available in the following GitHub repository: https://github.com/lidelejonagoitiagarmendia/Firn_densification.git